

Three-dimensional solutions for coating flow on a rotating horizontal cylinder: Theory and experiment

P. L. Evans,^{a)} L. W. Schwartz, and R. V. Roy

Department of Mechanical Engineering, University of Delaware, Newark, Delaware 19716

(Received 29 April 2004; accepted 14 April 2005; published online 24 June 2005)

We present three-dimensional numerical simulations of the flow of a thin liquid coating on a rotating horizontal right circular cylinder. The liquid motion is described using a lubrication model. The model evolution equation is discretized and solved numerically using an alternating-direction implicit algorithm. The cylinder rotates about its axis, carrying liquid around its circumference, resulting in the formation of a relatively thick coating where the cylinder surface moves upward. For coatings which are initially nearly uniform along the cylinder axis, this results in a ridge of liquid aligned with the cylinder axis. Over time, this ridge may break up into one of several possible configurations, including drops near the underside, and rings enveloping the cylinder. Simulations show that on larger cylinders, under certain circumstances this ridge may develop undulations which grow to form long fingers. These fingers drain down the cylinder. The simulation results are compared with a simple laboratory experiment, which exhibits similar fingering. © 2005 American Institute of Physics. [DOI: 10.1063/1.1942523]

I. INTRODUCTION

A cylinder undergoing uniform rotation about a horizontal axis is able to hold a thin coating of liquid, due to the combined effects of liquid viscosity and cylinder rotation. In general, however, the coating on a long right circular cylinder may be subject to instability due to the action of surface tension at the liquid-air interface, and centripetal acceleration. Analysis of this problem requires an understanding of the interplay between gravitational, rotational, and surface tension effects on the coating.

The development of axial variation of the coating thickness along the cylinder axis has been demonstrated in numerous experiments.¹⁻⁵ It has the potential to adversely affect many coating operations, such as the production of photographic film and aluminum foil. In the paper industry, this phenomenon occurs on the table rolls of a Fourdrinier machine.⁶ A similar instability in the phosphor coating inside fluorescent light tubes may lead to the production of a defective product.⁷ Improved knowledge of when instability occurs in such situations is quite valuable,⁵ as is an understanding of when a coating will fall from a slowly rotating roller or be flung from a rapidly rotating roller.

In determining whether coating will be retained on a rotating object, it is necessary to account for the tendency of an elongated volume of liquid to break into droplets under the influence of surface tension. Neglect of variation along the length of the object will lead to an incorrect prediction of the coating behavior. For a rotating body of arbitrary shape, the situation is more complicated; the current work provides the basis for modeling such objects.

Figure 1 shows the cylinder and the coating. The cylin-

der axis is held perpendicular to gravity, and the coordinate system does not rotate with the cylinder. Throughout this work, the cylinder rotation rate Ω , the coating viscosity μ , density ρ , and surface tension σ are all assumed constant. This simplification may not always be appropriate, for example, where the coating temperature varies, altering its physical properties.

Much of the prior work on this problem has been directed at the two-dimensional problem, in which variation along the cylinder axis is neglected. This restricted problem formed the subject of previous work by us.⁸ When axial variation is neglected, a simple model¹ including only cylinder rotation balanced by gravitational drainage is possible. For a coating thickness h , the liquid flux at any point is then given by

$$Q = R\Omega h - \frac{\rho g}{3\mu} h^3 \cos \theta, \quad (1)$$

where R is the cylinder radius, θ is measured as shown in Fig. 1, and g is acceleration due to gravity. In a steady state, Q is a constant which is independent of θ , leading to a cubic equation for h . The thickest coating occurs at $\theta=0$, where the upward flow due to rotation is most opposed by downward drainage. For a coating on the outside or inside of the cylinder, of mean thickness H , this model allows no steady solutions for rotation rates less than a critical value Ω_c , given by

$$\frac{\mu\Omega_c}{\rho g R} = \left(\frac{2\pi}{4.443} \right)^2 \left(\frac{H}{R} \right)^2. \quad (2)$$

Surface tension allows additional liquid to be supported, so that steady solutions may be found for $\Omega < \Omega_c$, and even for a stationary cylinder. In such cases the excess liquid forms a ridge on the cylinder underside.

^{a)}Present address: Institut für Mathematik, Humboldt-Universität zu Berlin, D-10099 Berlin, Germany. Electronic mail: pevans@mathematik.hu-berlin.de

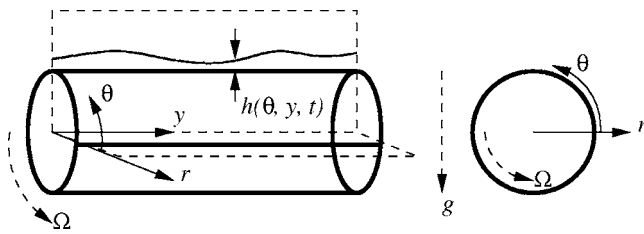


FIG. 1. The horizontal rotating cylinder and its coordinate system.

Work using the Stokes equation^{5,9} to determine the steady-state free surface, assuming no axial flow, but including surface tension, has demonstrated reasonable agreement between the full Stokes approximations and thin-film theory, when the requirements of the latter are met. Further work by Peterson *et al.*¹⁰ extends these results to low rotation rates at which lobes form prior to “load shedding,” but does not include axial variation.

For stationary liquid cylinders, it is well known that axial instabilities are possible. The critical wavelength for instability is $2\pi R$, with axial perturbations longer than this growing in amplitude. For a thin coating on a stationary wire,¹¹ the most rapidly growing disturbance has a wavelength $\lambda = (0.707)2\pi R$. For a large stationary cylinder held horizontal, the Rayleigh-Taylor instability destabilizes the coating underneath the cylinder. Depending on the cylinder diameter, either of these instabilities may affect the coating. This will be explored in more detail in Sec. III A. Numerical simulations of the coatings on stationary cylinders of a range of diameters have been carried out previously.¹²

A thin coating on a rotating cylinder, in the absence of gravity, is also linearly unstable to long-wavelength axisymmetric disturbances.⁶ This instability is a result of centripetal acceleration, and leads to the formation of rings. Yih⁶ computed the wavenumber k_* of the fastest-growing axial disturbance for a range of Reynolds numbers $\mathfrak{R} = \rho\Omega H_0^2/\mu$ and rotation rates, finding that k_* increases as the rotation rate is increased. For comparison with his experiments, Yih modified his theory by adding an *ad hoc* contribution to the pressure to account for the stabilizing effect of gravity at the top of the cylinder.

Observations of large axial variations in coatings include the bands seen by Kovac and Balmer,² which they named “hyrocysts,” finding that the number of bands per unit cylinder length increased approximately linearly with the cylinder rotation rate. Preziosi and Joseph⁴ incorporated axial flow into their model by using Moffatt’s lubrication flow solution in sections across the cylinder. The amount of liquid in each plane was determined by solving an axisymmetric problem. Their experiments showed good agreement with Moffatt’s maximum load criterion for thin enough layers. They suggest that axial variations are due to the competition between surface tension and centripetal acceleration, with gravity having a minor effect. However, at slow speeds, when the cylinder is nearly stationary, the non-axisymmetric Rayleigh-Taylor instability may lead to appreciable axial flow. The ribbing instability which interferes with roll coating operations¹³ is a related phenomenon.

A closely related situation arises when a liquid lines the inside of a cylindrical vessel undergoing rotation, known as “rimming.” In the rimming problem, when the rotation rate is below Ω_c , the liquid tends to pool as a “puddle” at the bottom of the cylinder. A coating-height discontinuity or stationary shock forms at slower speeds,^{14–16} which is smoothed by surface tension.

Rimming flows have displayed interesting axial variations, which have attracted attention.^{14,15,17,18} Thoroddsen and Mahadevan^{19,20} observed the formation of “shark teeth” along the cylinder axis in rimming experiments. The spacing of these shark teeth initially increases and then decreases as Ω is increased. They suggest that a mechanism similar to the fingering seen in flow down an inclined plane²¹ is responsible. They also found stationary and oscillating pendant structures which are not always evenly spaced, attributed to a balance between gravitational and viscous forces. Numerical modeling by Hosoi and Mahadevan²² using a simplified model equation for coating thickness shows features similar to the shark teeth reported above. Melo²³ has also shown interesting stationary bumps appearing in rimming flows at low speed. In some cases, axial variation can be so extreme that dislike structures form in which a free surface crosses the axis of the cylinder, dividing the air into separate cells or bubbles.^{4,24}

Boote and Thomas²⁵ presented a study of how the addition of small granules (solid spherical glass beads) to the liquid can alter the rotation rate at which transitions between various types of structures occur. At high particle loadings, particles accumulate in thicker bands, separated by thin almost-particle-free regions. The wavelength of these granular bands increased with Reynolds number $\mathfrak{R} = \rho\Omega R H/\mu$. The structure which appears depends on both \mathfrak{R} and particle volume fraction. Similar studies involving a suspension of neutrally buoyant rigid particles,²⁶ and sand²⁷ have been performed.

This paper reports on three-dimensional numerical simulations using a lubrication model for coating flow on a cylinder which rotates with constant angular velocity, which includes axial variation.⁸ Section II reviews the model and briefly describes an efficient numerical method for the model. Validation of the numerical method is presented in Sec. III, by comparing with the expected behavior in appropriate limiting cases. It is then used to perform simulations of coatings on rotating cylinders in Sec. IV. The key results arising from this work are as follows. There is a range of parameters in which steady three-dimensional solutions (in the laboratory frame of reference) occur. These range from drops beneath the cylinder at the slowest speeds to elongated structures which may wrap around the cylinder at higher speed, on small cylinders. There is a possibility of fingerlike structures on large (compared to the capillary length) cylinders. To support these results, a simple experiment was performed. This is described in Sec. V and the results are compared to simulations, which exhibits similar fingering. Section VI summarizes the results of this work.

II. COATING FLOW MODEL AND NUMERICAL SCHEME

Our model describes the liquid coating shown in Fig. 1 on the outer surface of a circular cylinder. The cylinder has radius R and rotates about its axis of revolution, which is held horizontal, at constant angular speed Ω . The coating is assumed to be an incompressible Newtonian liquid and completely wets the cylinder. It is subject to a no-slip boundary condition at the moving wall, stress conditions on the mov-

ing free surface, and a kinematic boundary condition which allows for updating the position of the free surface.

A. Lubrication model

Carrying out a perturbation expansion (see Appendix A) in the small parameter $\epsilon = H/R \ll 1$, where H is the characteristic film thickness, leads to an evolution equation for the coating thickness, $h(\theta, y, t)$. This is

$$(R+h)\frac{\partial h}{\partial t} = -R\Omega\frac{\partial}{\partial\theta}\left(h + \frac{h^2}{2R}\right) + \frac{\rho g}{\mu}\frac{\partial}{\partial\theta}\left[\left(\frac{h^3}{3} + \frac{h^4}{2R}\right)\cos\theta\right] - \frac{1}{R}\frac{\partial}{\partial\theta}\left\{\frac{\sigma h^3}{3\mu}\frac{\partial}{\partial\theta}\left(\frac{h}{R^2} + \nabla^2 h\right)\right\} + \frac{\rho h^3}{3\mu}(R\Omega^2 - g\sin\theta)\frac{\partial h}{\partial\theta} - R\frac{\partial}{\partial y}\left\{\frac{\sigma h^3}{3\mu}\frac{\partial}{\partial y}\left(\frac{h}{R^2} + \nabla^2 h\right) + \frac{\rho h^3}{3\mu}(R\Omega^2 - g\sin\theta)\frac{\partial h}{\partial y}\right\}, \quad (3)$$

where $\nabla^2 = R^{-2}(\partial^2/\partial\theta^2) + (\partial^2/\partial y^2)$ measures variation of h along the cylinder surface.

For use in a numerical scheme, it is convenient to write (3) in dimensionless form. We define the dimensionless viscosity M , dimensionless rotation rate W , and Bond number Bo by

$$M = \frac{\mu}{\rho\sqrt{g}R^3}, \quad W = \frac{\Omega}{\sqrt{g/R}}, \quad Bo = \frac{\rho g R^2}{\sigma}.$$

Using the scaling

$$\bar{h} = \frac{h}{\epsilon R}, \quad \bar{y} = \frac{y}{R}, \quad \bar{t} = \frac{\rho g H^2}{\mu R} t,$$

we obtain

$$(1 + \epsilon\bar{h})\frac{\partial\bar{h}}{\partial\bar{t}} = -U_\Omega\frac{\partial}{\partial\theta}\left(\bar{h} + \epsilon\frac{\bar{h}^2}{2}\right) + \frac{\partial}{\partial\theta}\left[\left(\frac{\bar{h}^3}{3} + \epsilon\frac{\bar{h}^4}{2}\right)\cos\theta\right] - \epsilon\bar{\nabla} \cdot \left\{\frac{\bar{h}^3}{3Bo}\bar{\nabla}(\bar{h} + \bar{\nabla}^2\bar{h}) + \frac{\bar{h}^3}{3}[W^2 - \sin\theta]\bar{\nabla}\bar{h}\right\}, \quad (4)$$

where $\bar{\nabla} = \mathbf{e}_\theta(\partial/\partial\theta) + \mathbf{e}_y(\partial/\partial\bar{y})$ and $\bar{\nabla}^2 = (\partial^2/\partial\theta^2) + (\partial^2/\partial\bar{y}^2)$. The quantity $U_\Omega = MW\epsilon^{-2}$ is the ratio of the wall speed $R\Omega$ to the velocity scale $U = \rho g H^2/\mu$. For the coatings of interest here, U_Ω is of $O\{1\}$ or smaller. The behavior of the coating is determined by the four dimensionless parameters M , W^2 , Bo , and ϵ , together with the initial conditions. Equation (4) is applicable when $\epsilon \ll 1$, and MW/ϵ^2 and W^2 are of $O\{1\}$ or smaller.

Axial flow in (4) arises naturally from pressure differences produced by thickness variation along the cylinder axis. The effects of rotation, gravitation and surface tension all contribute to this pressure gradient. For a nonrotating cylinder, (4) is consistent with the evolution equation obtained

by Weidner *et al.*¹² When terms of order ϵ in (4) are neglected, it becomes the time-dependent version of (1), obtained by Moffatt.¹

B. Numerical method

After rescaling so that all lengths, including coating thickness, are measured in units of R , the coating evolution equation becomes

$$(1+h)\frac{\partial h}{\partial t} = -MW\frac{\partial}{\partial\theta}\left(h + \frac{h^2}{2}\right) + \frac{\partial}{\partial\theta}\left[\left(\frac{h^3}{3} + \frac{h^4}{2}\right)\cos\theta\right] - \nabla \cdot \left\{\frac{h^3}{3Bo}\nabla(h + \nabla^2 h) + \frac{h^3}{3}[W^2 - \sin\theta]\nabla h\right\}. \quad (5)$$

Simulations typically begin with a coating layer of thickness $h(\theta, y, 0) \approx \epsilon R$, and ϵ only serves to set the scale of the initial condition.

When the coating layer is sufficiently thin, it is appropriate to simplify Eq. (5) by neglecting several small terms of order ϵ which arise due to the curvature of the cylinder surface. Neglect of the second term on the left-hand side of (5), $h\partial h/\partial t$, is then also appropriate, and simplifies the numerical scheme. Provided ϵ is small enough, neglect of these terms will not qualitatively change the results obtained. The simplified coating evolution equation becomes

$$\frac{\partial h}{\partial t} = -MW\frac{\partial h}{\partial\theta} + \frac{\partial}{\partial\theta}\left(\frac{h^3}{3}\cos\theta\right) - \nabla \cdot \left\{\frac{h^3}{3Bo}\nabla(h + \nabla^2 h) + \frac{h^3}{3}[W^2 - \sin\theta]\nabla h\right\}. \quad (6)$$

The remaining terms in (6) contain all the essential physics of the problem including ‘‘dragging’’ of liquid by rotation, and drainage due to the azimuthal and radial components of

gravity. Retaining surface tension terms is particularly important, as these terms become important in regions where there are large changes in coating thickness.²⁸

An alternating direction implicit finite-difference method, described in Appendix B, is used to solve either the nonlinear equation (5) and (6). The (θ, y) domain is discretized in the θ and y directions, into a mesh of $n \times (n_2 + 1)$ grid points, with a uniform grid spacing $\Delta = 2\pi/n$ and length $L = n_2\Delta$. At the end surfaces $y=0$ and $y=L$ reflection symmetry, or zero flux, boundary conditions are imposed; periodicity is imposed in the θ direction.

III. MODEL VALIDATION

In this section the numerical method is tested in the case when gravity is negligible, so that the coating is axisymmetric. Next, with gravity restored, but the cylinder held stationary, our simulations are compared with existing numerical results. Before doing so we review two common types of coating instability.

A. Coating instabilities

At least two competing instabilities potentially influence the coatings considered here. Both instabilities exist for a stationary cylinder, and it is to be expected that they, and potentially other instabilities, will continue to affect the coating when the cylinder is rotating.

The axisymmetric *Rayleigh sausage* instability²⁹ applies to any cylindrical column or jet of liquid, solely as a result of its tendency to minimize surface area. For the stationary case¹¹ the coating is unstable to waves of wavelength greater than $2\pi a$ where $a = R + h_0$ is the outer radius of the coating, and the fastest growing wavelength is proportional to the cylinder radius R . Below we present a simplified analysis based on lubrication theory, including cylinder rotation.

When gravity is absent, the coating profile is axisymmetric, and the evolution equation (3) becomes

$$\frac{\partial h}{\partial t} = -\frac{R}{R+h} \frac{\partial}{\partial y} \left\{ \frac{\sigma h^3}{3\mu} \frac{\partial}{\partial y} \left(\frac{h}{R^2} + \frac{\partial^2 h}{\partial y^2} \right) + \rho R \Omega^2 \frac{h^3}{3\mu} \frac{\partial h}{\partial y} \right\}. \quad (7)$$

The uniform coating $h=h_0$ is unstable if a small axisymmetric perturbation of h , of the form

$$h(y, t) = h_0 + \alpha e^{\omega t} \cos ky, \quad (8)$$

grows in amplitude. Substituting into (7) and linearizing gives the growth rate of these disturbances,

$$\omega = \frac{R}{R+h_0} \frac{\sigma h_0^3}{3\mu} \left([1+S] \frac{k^2}{R^2} - k^4 \right), \quad (9)$$

where $S = \rho \Omega^2 R^3 / \sigma$. Disturbances of wavelength less than the cutoff wavelength

$$\lambda_0 = \frac{2\pi R}{\sqrt{1+S}} \quad (10)$$

will decay, while longer wavelength disturbances will grow. The wavelength of the fastest-growing disturbance and its growth rate are

$$\lambda_{\text{axi}} = \frac{2\sqrt{2}\pi R}{\sqrt{1+S}},$$

$$\omega_{\text{axi}} = \frac{\sigma h_0^3}{12\mu R^3 (R+h_0)} [1+S]^2. \quad (11)$$

Provided that the effects of gravity are negligible, i.e., when $\text{Bo} \ll 1$, the coating on a long cylinder should become unstable, with disturbances tending to have initial wavelength λ_{axi} .

On a rotating cylinder, the wavelength of axisymmetric disturbances may be significantly reduced on rotating cylinders, if S is large. In reported experiments, S varies widely, from 0.1 to 0.2 in the experiments by Preziosi and Joseph⁴ and Kelmanson,⁵ to 10^5 or more in Yih's experiments.⁶ In this work, the largest value of S considered will be about 1.6 when $\text{Bo} = 500$ and $W \sim 0.056$, so in this case the wavelength and the growth rate of this instability may be appreciably modified.

The second Rayleigh-Taylor instability^{29,30} is caused by the combined effects of surface tension and gravity. Gravity has a destabilizing effect on a layer of dense liquid which is above less-dense surrounding atmosphere. This leads to the formation of drops on the underside of a flat plate, which are supported by surface tension. In the present problem, this instability acts at the cylinder underside. On the top of the cylinder, gravity stabilizes the coating.

The stability of a layer subject to small disturbances may be determined by considering a thin film underneath a horizontal plane. In this case

$$\frac{\partial h}{\partial t} = -\frac{\partial}{\partial y} \left\{ \frac{h^3}{3\mu} \left[\sigma \frac{\partial^3 h}{\partial y^3} + \rho g \frac{\partial h}{\partial y} \right] \right\}. \quad (12)$$

For a small periodic perturbation of the coating, (8), the disturbance growth rate is

$$\omega = \frac{\sigma h_0^3}{3\mu} \left(\frac{k^2}{l_c^2} - k^4 \right), \quad (13)$$

where $l_c = \sqrt{\sigma / (\rho g)}$ is the capillary length. Positive growth rates occur for wavelengths $\lambda = 2\pi/k$ longer than

$$\lambda_0 = 2\pi l_c,$$

while shorter wavelength disturbances are damped by surface tension. The fastest-growing disturbance wavelength and the growth rate are

$$\lambda_{\text{RT}} = 2\sqrt{2}\pi l_c,$$

$$\omega_{\text{RT}} = \frac{\sigma h_0^3}{12\mu l_c^4}.$$

Comparing (9) and (13), it is apparent that when $h_0 \ll R$ and $R/l_c > \sqrt{1+S}$ the Rayleigh-Taylor instability will have a faster growth rate. For large cylinders and moderate S , the observed instability wavelength should scale with l_c , while for small cylinders, the axisymmetric Rayleigh instability should dominate, with a wavelength scaling with R . For cylinders of intermediate size, for which $\text{Bo} \sim 1$, a transition

TABLE I. Properties of the cylinder and silicone oil used for experiments.

Property, symbol	Value
Cylinder radius, R	3.4 cm
Length, L	27.9 cm
Rotation rate, Ω	$<2\pi \text{ s}^{-1}$
Coating surface tension, σ	24.5 dyn/cm
Viscosity, μ	0.48 P
Density, ρ	0.96 g/cm ³

between these two instabilities occurs. Experiments by de Bruyn³¹ have demonstrated this, though with considerable experimental variation in wavelength around the theoretical values.

B. Axisymmetric coatings

The numerical method was first tested with g set to zero. In this case, an initially axisymmetric coating should remain axisymmetric, but be unstable to the Rayleigh sausage instability. Simulations were performed using (5) with a computational domain of length $\lambda/2$ and the initial condition

$$h(\theta, y, 0) = \epsilon + \alpha_0 \cos\left(\frac{2\pi y}{\lambda}\right) \quad (14)$$

corresponding to a half-cosine variation in the axial direction. Simulations were performed for $S=0$ and $S=1$, with $\epsilon = 0.1$, $\alpha_0 = 0.001$, and dimensionless grid spacing $\Delta = \pi R/10$. The wavelength was varied between $1.25\pi R$ and $10\pi R$. Growth rates for the disturbance in the numerical model were estimated by assuming that the coating profile remained of the form (8). The estimate for the growth rate is then

$$\omega_{\text{est}} = \frac{1}{t} \log \frac{h_{\text{max}} - h_{\text{min}}}{2\alpha_0},$$

where h_{min} and h_{max} are the minimum and maximum values of h attained by the numerical solution at time t . The numerical solutions remained axisymmetric, with numerical growth rates in agreement with those predicted by (9).

When the cylinder is rotating, the linearized theory above predicts faster growth at small wavelengths. To demonstrate this, we simulated a cylinder of length $L = 5\pi R$, and $n=20$ and $n_2=50$, for both $S=0$ and $S=1$. The cutoff wavenumber is $Rk=1$ for the stationary cylinder and $Rk=\sqrt{2}$ for $S=1$. For the cylinder and silicone oil used in the experiments of Sec. V (see Table I), $S=1$ represents a rotation rate of 0.025 s^{-1} .

The initial coating is nearly uniform, with small-amplitude random noise added:

$$h(\theta, y, 0) = \epsilon + \alpha_0 \left[R_y - \frac{1}{2} \right], \quad (15)$$

where R_y denotes a random value chosen uniformly between 0 and 1 for each value of y corresponding to a grid point. Allowing R to also vary with θ produces similar results.

While the disturbance amplitude remains small, its growth is linear and h has a generally sinusoidal profile. Figure 2 shows that the coating thickness variation h_{max}

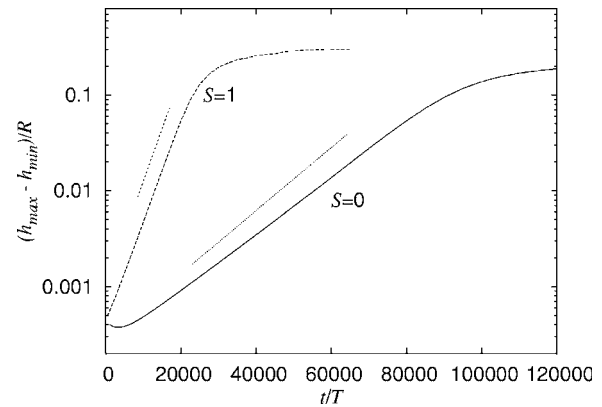


FIG. 2. For an axisymmetric coating, instability is present on both a stationary cylinder ($S=0$) and a rotating cylinder ($S=1$). Coating thickness variation grows for a nearly-uniform initial coating, with mean thickness 0.1 and random noise of amplitude $0.001R$. The thickness variation increases faster for a rotating cylinder. Growth rates are close to those of the fastest-growing modes from the theory of Sec. III A, shown as straight lines.

$-h_{\text{min}}$ first decreases from its initial value of $\alpha_0 = 0.001$, as the noisy initial condition is smoothed. Once growth is underway, it is at a rate close to ω_{axi} , indicated by the lower straight line in Figure 2.

Figure 3 shows the development of the coating profile when $S=1$. The growth rate is now four times larger than for $S=0$. Initially nearly three complete waves fit in the domain. The symmetry boundary conditions force the coating to have a peak or trough at both boundaries, so the actual number of waves must be an integer or half integer. As variations in h become large at later times, nonlinear effects become important. The waves coalesce, leaving two relatively pronounced troughs at $y \approx \pi$ and $y \approx 4\pi$. These restrict flow, slowing further thinning at the troughs, until eventually small “satellite” drops form there. The drops become isolated as the coating thickness between them approaches zero.

In comparison, a run with a stationary cylinder ($S=0$) leads to only a little over $1\frac{1}{2}$ full wavelengths forming. This is close to the number of waves expected if the disturbance has the fastest growing wavelength λ_{axi} , which would pro-

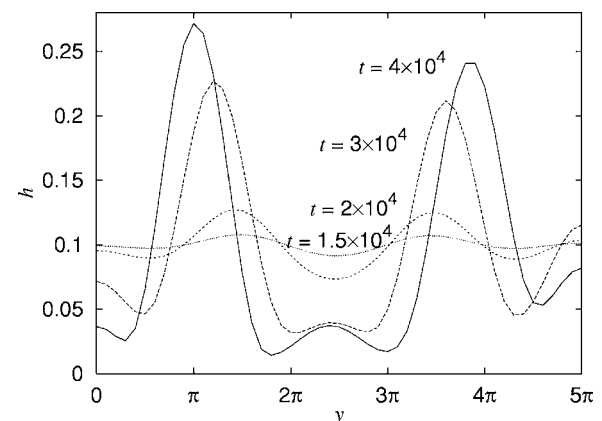


FIG. 3. Growth of a disturbance on a rotating cylinder with $S=1$, computed using the axisymmetric model. Small-amplitude random noise applied to the initial coating drives the instability. The coating profile $h(y)$ is shown at the indicated times.

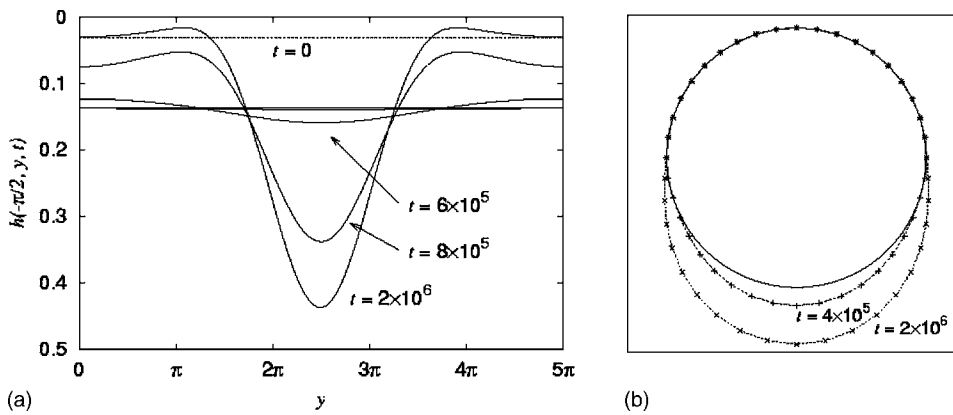


FIG. 4. Film thickness for a small stationary cylinder, with $Bo=1$, and $\epsilon=0.03162$. (a) On the underside ($\theta=3\pi/2$), at $t=(2,4,6,8) \times 10^5$ and $t=2 \times 10^6$. (b) Cross section at $y=7.9$, at $t=4 \times 10^5$ (+) and 2×10^6 (x). At the earlier times there is little axial variation; by the later times shown, a large drop has developed.

duce $5\pi/(2\sqrt{2}\pi) \approx 1.8$ full waves. Rotation shortens the preferred wavelength for breakup of the coating. Similar growth rates [with $R+h_0$ replaced by R in (11)] and long-time evolution of the coating were found in simulations using the simplified model (6) instead of (5).

C. Stationary cylinders

In this section, the model is tested for a stationary cylinder with gravity included ($W=0$, $g>0$). In this situation, viscosity can be absorbed into the time scale. Time is measured in units of $\mu/\rho g R$ and lengths in units of R . With these changes, (4) becomes

$$(1+h) \frac{\partial h}{\partial t} = \frac{\partial}{\partial \theta} \left[\left(\frac{h^3}{3} + \frac{h^4}{2} \right) \cos \theta \right] - \nabla \cdot \left\{ \frac{h^3}{3Bo} \nabla (h + \nabla^2 h) - \frac{h^3}{3} \sin \theta \nabla h \right\}. \quad (16)$$

The dynamics of the flow can be characterized by just two parameters ϵ and Bo . Since the present model is restricted to small ϵ , this leaves Bo as the remaining free parameter. For a given liquid, varying Bo represents changing the cylinder size.

Weidner *et al.*¹² describe the drainage behavior of a coating on a stationary cylinder in four phases.

Phase 1. Gravity-driven drainage toward the cylinder underside from the top and sides. A “ridge” of liquid forms at $\theta=3\pi/2$.

Phase 2. Drainage slows and a small-amplitude disturbance develops along the length of the ridge.

Phase 3. As the amplitude of this disturbance grows, growth becomes nonlinear. In the troughs, secondary drops become apparent.

Phase 4. Evolution slows down due to the thin coating everywhere except in the drops, which continue to accumulate liquid. There may be additional drop movement and coalescence, before reaching a steady state.

Our three-dimensional numerical method was first tested by comparison with the problem presented in detail by Weidner *et al.*,¹² for which $R=l_c$ and $\epsilon=0.1$. An initial layer of thickness $h \approx 0.1R$, with random noise of 1% of the mean thickness in both the θ and y directions, was allowed to drain on a stationary cylinder. A mesh of 40×100 grid points was used on a cylinder of length $L=5\pi R$.

Our results, using both (16) and (6) with $W=0$, are similar to those of Weidner *et al.* at early times, and are not included here. In particular, we find the same value for the initial disturbance wavelength, $\lambda \approx 10.5$ (exactly two-thirds of the domain length), compared to the value $2\pi\sqrt{2} \approx 8.89$ predicted for both the axisymmetric Rayleigh and Rayleigh-Taylor instabilities, since $R=l_c$ in this case.

By phase 4, however, coating thicknesses exceed one cylinder radius at the peaks. Up to this point, there is reasonable agreement between our results and those of Weidner *et al.* The current lubrication model loses accuracy here, as our numerical method approximates the full nonlinear expressions for free surface curvature and, in the case of (16), mass conservation. These are important for coating thicknesses $h \sim R$ or larger, and particularly when $R \sim l_c$ or smaller. As a result, thick coatings, such as occur in the large drops in this case, are not well modeled. This introduces quite large errors when compared to true static drop shapes. As we have shown previously,⁸ the simplified model (6) is appropriate when ϵ is sufficiently small. Furthermore, rotation tends to reduce extremes of coating thickness, so the present model should be more appropriate when $W \neq 0$. In the remainder of this work, thinner coatings, for which the current thin-film model has better validity, are examined on cylinders of varying radius.

With the initial coating thickness reduced to $l_c/\sqrt{1000}$ on the same cylinder ($R=1$, $Bo=1$, $\epsilon=0.03162$), the coating profile on the underside of the cylinder in Fig. 4(a) shows a behavior similar to that already seen by Weidner *et al.* Liquid initially drains to form a ridge beneath the cylinder. A transverse wave develops, which rapidly increases in amplitude. The wave grows to form the nucleus of a large drop, with smaller satellite drops on each side. Figure 4(b) shows cross sections of the coating at two times. For this small-diameter cylinder, at the earlier time shown the ridge extends about halfway around the cylinder circumference. The ridge develops ripples along its length, which become distinct drops over time. A cross section across a developed drop at a later time is also shown. In simulations of smaller cylinders (e.g., $Bo=0.1$) these drops wrap nearly the entire way around the cylinder or even form annular beads. Such cylinders, with diameter less than a millimeter for typical liquids and terrestrial gravity, are not of primary interest here.

A large cylinder, with $R=10l_c$ ($Bo=100$) was also studied. This size, corresponding to a cylinder diameter of sev-

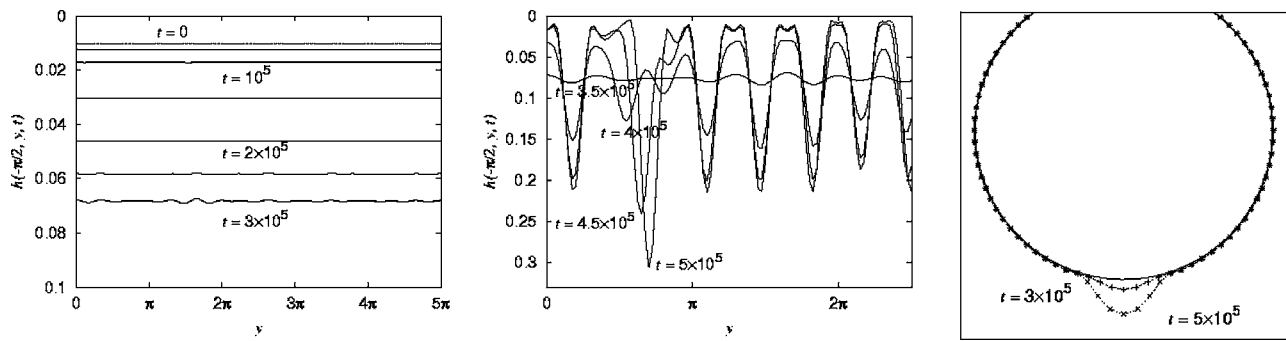


FIG. 5. On a large stationary cylinder, the ridge beneath the cylinder breaks up with a comparatively short wavelength. Coating thickness on the underside, for $Bo=100$ and $\epsilon=0.01$, at (a) $t=(0.5, 1, \dots, 3) \times 10^5$; (b) $t=(3.5, 4, 4.5, 5) \times 10^5$. (c) Cross sections at $y=7.9$ have little axial variation at early times ($t=3 \times 10^5$, +); later, a drop develops ($t=5 \times 10^5$, \times).

eral centimeters, is similar to that which have been used in previous experiments.^{1,4} To resolve features adequately, the grid spacing was reduced, so $n=80$ and $n_2=200$. A coating thickness of $0.1l_c$ ($\epsilon=0.01$) was used. Figure 5(a) shows many ripples appearing on the underside of the coating as the liquid drains here from the top and sides of the cylinder. These ripples grow to form droplets. At the earliest time there are at least 15 ripples, though several coalesce, leaving only 13 which grow into drops. Based on a fastest-growing wavelength of $2\sqrt{2}l_c$, about 17.7 waves would be expected. Only the left-hand portion of the cylinder ($0 < y < 2.5\pi$) is shown in Fig. 5(b), showing profiles at later times. Two small ripples near $y=\pi$ can be seen merging to form a single large drop. In the large space created to either side, relatively large secondary drops are able to form. For these large cylinders, the axially uniform liquid ridge, and the later drops, only occupy a small portion of the underside of the cylinder. Cross sections of the cylinder, shown before and after breakup in Fig. 5(c), when compared to Fig. 4(b), show this clearly.

At the last time shown in Fig. 5, $t=5 \times 10^5$, the largest coating thickness shown, $0.3R$, or $3l_c$, is thicker than that of the largest possible static drop beneath a flat plate.³² Such a large volume of liquid could not be supported in reality and would break off as a drop. Although the numerical method continues to produce solutions beyond this time, such solutions are therefore somewhat nonphysical.

For the $Bo=100$ simulations (and simulations with $Bo=10$, not shown here) we observed somewhat fewer waves than predicted on the basis of the Rayleigh-Taylor wavelength $2\sqrt{2}l_c$. This is not unexpected, however, as that result applies for a two-dimensional coating, and ignores curvature in the third direction on the underside. The finite axial length of the domain also influences the results. For small-amplitude waves, we (and Weidner *et al.*) find $\lambda \approx 8.9$ (the expected value), when $Bo=1$, only for much longer cylinders than considered here, with longer wavelengths for short cylinders. The relatively coarse grid spacing may also be a factor. For the $Bo=100$ simulation, there are only about 13 grid points per wave, and each large drop occupies only about nine grid points in each direction. However, runs using (6) for $Bo=100$ with a longer cylinder length, and with reduced grid spacing, continue to give a spacing between peaks

which vary (nonsystematically) between $10.9l_c$ and $12.5l_c$. Furthermore, coalescence reduces the number of drops, increasing their wavelength. The final number of drops will therefore tend to correspond to a wavelength longer than that of the fastest-growing linear disturbance. Finally, in simulations involving a random initial condition, growth need not occur with precisely the fastest wavelength, but with some variation around it. Experiments³¹ measuring the wavelength of drops on wires have exhibited a considerable variation in drop spacing within a single experiment, with a standard deviation of 15%–20% of the mean value.

In this section, we have demonstrated that the numerical method for both (5) and (6) produces the expected behavior for a coating on a stationary cylinder, subject to gravitational drainage. The qualitative effect of a change of cylinder size, relative to the capillary length l_c , was considered. The same basic pattern of behavior is repeated for each cylinder size. Following an initial period of axially uniform drainage, a ridge forms on the cylinder underside. This ridge is unstable and ripples appear on it. Liquid drains from thinner to thicker parts, causing the ripples to grow into distinct droplets. Secondary satellite drops then form between the main drops. Similar evolution will be seen in the rotating case, in the following section. The ripple wavelength depends on the Bond number. For the cylinders considered here, with radius of the order of the capillary length l_c or larger, the disturbance wavelength is dependent on l_c ; for small cylinders it is determined by the cylinder radius.

While the coating remains thin, the model produces results similar to those seen previously.¹² Once thickness grows to be comparable with the cylinder radius, we expect inaccuracy, similar to that observed for two-dimensional static drops. The excessive growth to nonphysical thickness seen here would be prevented by using full curvature. On rotating cylinders, for which coating thicknesses tend to be less large, thickness growth will be a less severe limitation of the current model.

IV. ROTATING CYLINDERS

Of the wide range of configurations offered by the four parameters, ϵ , Bo , M , and W , just two families are considered here. These are obtained by fixing the cylinder size, and

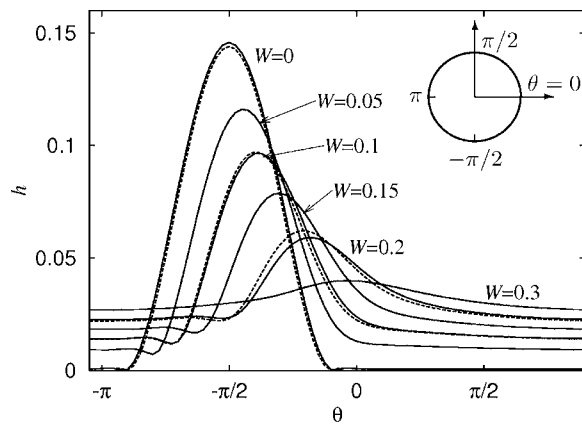


FIG. 6. “Unwrapped” steady two-dimensional (axially uniform) coating profiles $h(\theta)$ for the small rotating cylinder considered in Sec. IV A. Here W is varied, while $Bo=1$, $\epsilon=0.031\ 62$, and $M=0.007$. Solid lines show solutions computed using (6); dashed lines show that the effect of retaining the additional terms in (5) is small, for $W=0, 0.1$, and 0.2 .

the coating physical properties and thickness (and thus Bo , ϵ , and M) for a small cylinder and a large cylinder. In each case, the effect of varying the rotation rate at speeds below Ω_c is observed.

A. Small cylinders: $Bo=1$

We begin with the small cylinder, with $R=l_c$ ($Bo=1$), and use the same values for ϵ and M as were used in Sec. III C, namely $0.031\ 62$ and 0.007 , respectively. These parameters correspond, for example, to a water-glycerine mixture of 35% glycerine at $20\ ^\circ\text{C}$, which has a viscosity $\mu \approx 0.031\ \text{P}$, density $\rho \approx 1.09\ \text{g/cm}^3$, and surface tension $\sigma \approx 71.5\ \text{dyn/cm}$.³³ For terrestrial gravity this represents a cylinder diameter of $2l_c=5.2\ \text{mm}$. The Moffatt critical rotation rate is $\Omega_c=18\ \text{s}^{-1}$, giving $W_c=0.287$.

Steady solutions obtained using our previous two-dimensional model⁸ with $n=80$ are shown for $W=0.05, 0.1, 0.15, 0.2$, and 0.3 , which is slightly above W_c , in Fig. 6.

Because the cylinder is quite small, the coating is strongly influenced by surface tension, and the resulting profiles are difficult to distinguish when plotted in polar coordinates. In Fig. 6 the cylinder is “unwrapped” to better show h as a function of θ . At low speeds, a large drop forms close to the bottom of the cylinder. At higher speeds the solution is somewhat front-like, with a reduced bulge of liquid continually draining down the upward-moving part of the cylinder. Immediately below this bulge is an “undershoot” region. When W is near W_c , the coating becomes quite smooth, similar to the Moffatt solution.

The small terms neglected in solving (6) instead of (5) do not qualitatively alter the coating behavior. We show this using the two-dimensional variant of our model. Steady-state solutions of (5) are shown for $W=0, 0.1$, and 0.2 by dashed lines in Fig. 6. Solutions of (6), shown by solid lines in the figure, differ only slightly from these.

For $Bo=1$, both the axisymmetric and the Rayleigh-Taylor instabilities are present for cylinders longer than $2\pi R$, with the fastest-growing wavelength $\lambda=2\sqrt{2}\pi R$. We performed three-dimensional simulations on a cylinder of length $5\pi R$, with the expectation that the coating will be affected by both instabilities. The initial coating is a nearly uniform layer, with small random noise as in Sec. III C,

$$h(\theta, y, 0) = \epsilon \left(1 + 0.01 \left[R_{\theta, y} - \frac{1}{2} \right] \right), \quad (17)$$

where $R_{\theta, y}$ is a randomly chosen value between 0 and 1 for each value of θ and y corresponding to a grid point. To adequately resolve the sharp undershoot region seen below the main drop, a grid with $n=80$ and $n_2=200$ was used.

We first present results of a three-dimensional simulation using (5) with $W=0.1$, well below W_c . The coating at first evolves with virtually no variation across its length, closely matching the behavior of the two-dimensional solution. By $t=2 \times 10^5$, the coating profile is essentially the same as the final steady-state profile obtained with the two-dimensional model. There is a thick ridge of liquid with a peak at $\theta \approx 5.1$. This is shown somewhat later at $t=8 \times 10^5$ in Figs.

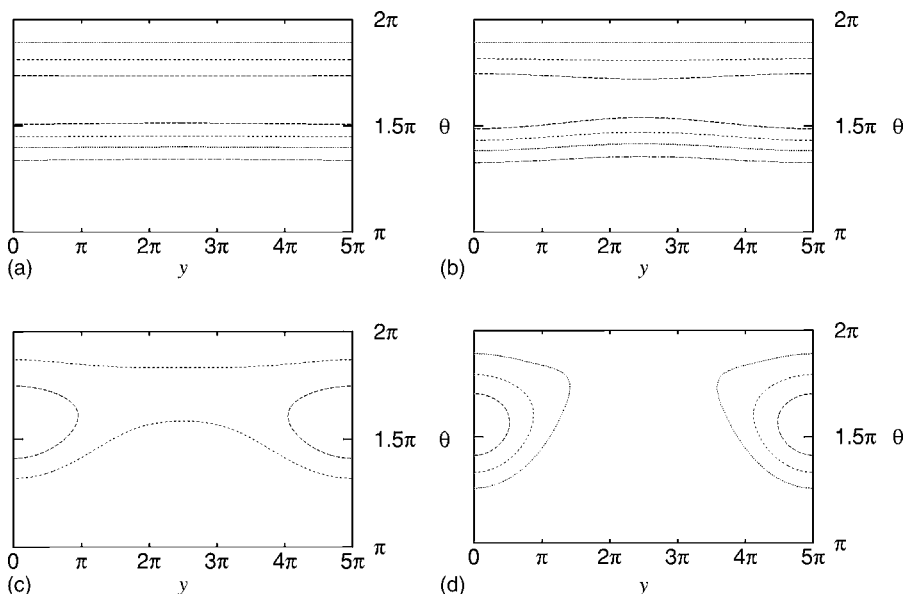


FIG. 7. Coating thickness at the lower portion of a small rotating cylinder obtained using the three-dimensional numerical method. The cylinder length $5\pi R$ is larger than the cut-off wavelengths of both the axisymmetric instability, $\lambda_{\text{axi}}^c = 2\pi R/\sqrt{1+S} = 1.99\pi R$, and the Rayleigh-Taylor instability, $\lambda_{\text{RT}}^c = 2\pi l_c = 2\pi R$. The initial ridge of liquid breaks up to form drops. As a contour plot ($\pi \leq \theta \leq 2\pi$), for (a) $t = 0.8 \times 10^6$; (b) $t = 1.2 \times 10^6$; (c) $t = 1.6 \times 10^6$; and (d) $t = 2.0 \times 10^6$. The contour interval is 0.02 in (a) and (b), and 0.05 in (c) and (d). Here $W=0.1$, $Bo=1$, $\epsilon=0.031\ 62$, and $M=0.007$.

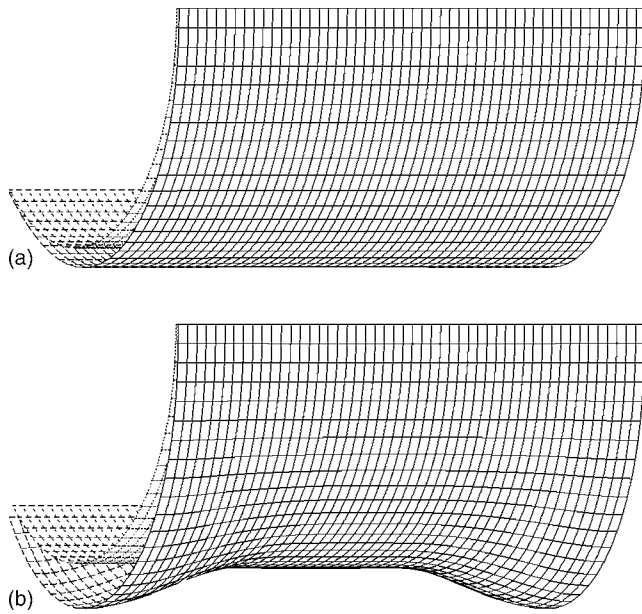


FIG. 8. The same coating as in Fig. 7, shown in perspective view (for $4 \leq \theta \leq 2\pi$), at (a) $t=0.8 \times 10^6$ and (b) $t=2.0 \times 10^6$.

7(a) and 8(a). Some slight axial variation, a remnant of the initial random perturbation, is still present. This leads to the appearance of a wavelike disturbance along the ridge by $t = 1.2 \times 10^6$, shown in Fig. 7(b). The disturbance then rapidly grows in amplitude until two distinct half drops are visible at $t = 1.6 \times 10^6$, joined by a much thinner ridge of liquid, seen in Fig. 7(c). These drops are distorted and shifted somewhat towards the upward-moving side of the cylinder. Liquid continues to drain into these drops, though more slowly. After $t \sim 2 \times 10^6$ [Figs. 7(d) and 8(b)], there is very little subsequent change in the coating profile, though liquid continues to slowly accumulate in the bulges.

As these drops develop, liquid is redistributed along the cylinder. This is evident as a change in the area of enclosed liquid in sections perpendicular to the cylinder axis. Figure 9 shows this area, computed as

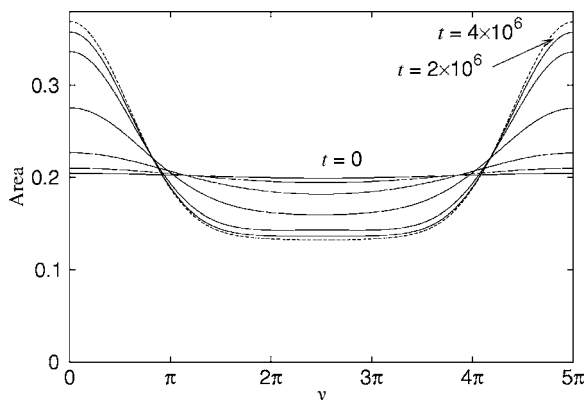


FIG. 9. Changes in the area of cylinder cross sections with time for the simulation shown in Fig. 7. As drops form, the liquid is redistributed along the cylinder. Shown at $t=(1.0, 1.2, \dots, 2.0) \times 10^6$ and $t=4.0 \times 10^6$, dashed.

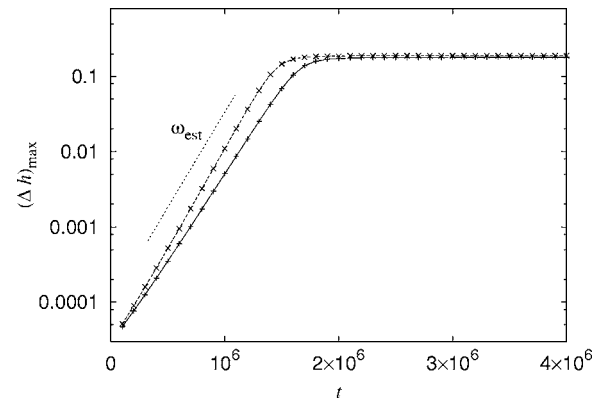


FIG. 10. The growth of axial variation of the coating for the simulation shown in Fig. 7, using (5) (+ symbols) and using the simplified model (6) (× symbols). The largest azimuthal variation $(\Delta h)_{\max}$ is defined by Eq. (18). The growth before $t=1.6 \times 10^6$ is essentially exponential, but stops when drop formation is complete. A growth rate ω_{est} may be estimated from the slope in the initial phase.

$$A_j = \sum_{0 \leq i < n} h_{i,j}^{(k)}$$

at $y=j\Delta$, at various times. The rapid change apparent for $1.4 \times 10^6 < t < 2.0 \times 10^6$ coincides with the period of drop formation. Another way to see the relatively rapid breakup is by the development of variation in thickness along the cylinder axis. The quantity

$$(\Delta h)_{\max} = \max_{0 \leq i < n} \{ \max_{0 \leq j \leq n_2} h_{i,j}^{(k)} - \min_{0 \leq j \leq n_2} h_{i,j}^{(k)} \} \quad (18)$$

measures the greatest variation along any line of constant θ at a given time. This quantity is shown in Fig. 10 on a logarithmic scale. The constant slope indicates exponential growth, characteristic of such disturbances.^{21,34,35}

This provides a measure of the growth rate of the instability $\omega_{\text{est}} \approx 5.8 \times 10^{-6}$ for this particular set of parameters Bo , ϵ , M , W , and domain length. Using (6) instead of (5) a slightly larger growth rate of 6.0×10^{-6} was found, as shown by the line marked with “×” symbols in Fig. 10. In comparison, the fastest-growing modes of the axisymmetric and Rayleigh-Taylor instabilities have growth rates (in units of $1/T$) of $\omega_{\text{axi}}=2.69 \times 10^{-6}$ and $\omega_{\text{RT}}=2.63 \times 10^{-6}$, respectively. The growth rate for the axisymmetric instability was calculated with $S=W^2Bo=0.01$. The effect of centrifugal acceleration is small at this low rotation rate. These growth rates are somewhat smaller than those observed.

The coating appearance differs considerably at other rotation rates. Figures 11(a)–11(d) show a series of contour plots of coating thickness after the drops have formed for $W=0, 0.05, 0.15$, and 0.2 , computed using (5). These “footprints,” together with Fig. 7(d) for $W=0.1$, reveal a change in drop shape with W . For slowly rotating cylinders, nearly circular drops form at the underside. As speed is increased, these are distorted and located somewhat up the upward-moving side of the cylinder. At the highest speed shown, $W=0.2$, the coating does not break up into droplets, but retains the shape of the two-dimensional solution. This last result will be considered shortly. Very similar results were

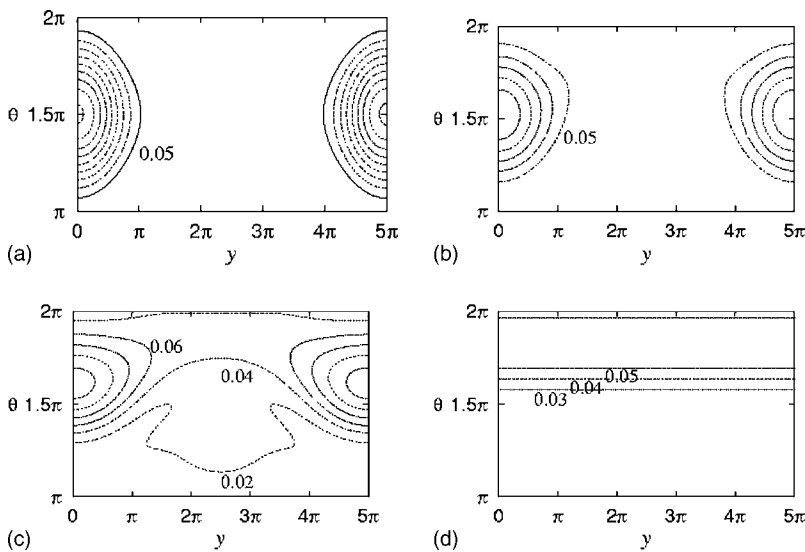


FIG. 11. Contour plots of coating thickness after drop formation is complete, as the rotation rate is varied. In (a) the cylinder is stationary ($W=0$). In (b) $W=0.05$ and in (c) $W=0.15$. For $W=0.2$, shown in (d) at $t=4 \times 10^6$, the coating does not break into drops. Here $Bo=1$, $\epsilon=0.03162$, $M=0.007$.

found using the simplified model (6) for each value of W . In the remainder of this section, we show only results computed using my (6).

The increase in extreme values of coating thickness, which accompanies breakup of the coating, is more gradual and occurs later for faster-rotating cylinders. This is seen in Fig. 12, showing the changes in maximum and minimum values of h over time for several values of W . In the figure, data points corresponding to the same value of W have been joined by interpolating splines. After breakup, there are still moderate amounts of liquid everywhere on the rotating cylinder, including the upper side, while on the stationary cylinder the upper surfaces retain very little liquid. This illustrates the tendency of rotation to smooth the coating. For $W=0.17$, there is little sign of breakup, even though it is a little over half the critical value W_c .

For W above about 0.18, the profile did not break up even after a long time. A plot of the distribution of cross-sectional area with time, similar to Fig. 9, indicates that after initially appearing to form a coherent disturbance, this disturbance decays in amplitude, leaving an axially uniform coating. To explore this, simulations using (6) with the half-cosine initial condition (14) were run for $W=0.2$, with α_0

$=0.01\epsilon$ and $\lambda=(5, 10, 15, 20)\pi R$. As the computational domain becomes large, such simulations become time consuming, posing a practical limit on the largest wavelength which may be tested. Intriguingly, the coating becomes more axially uniform over time, at all wavelengths tested, with shorter wavelengths producing a more uniform coating at a given time. Once the front has been established, the maximum axial variation $(\Delta h)_{\max}$ occurs at $\theta=5.34$ for this value of W . In Fig. 13, $(\Delta h)_{\max}$ is shown at various times for $\lambda=5\pi R$ and $10\pi R$. The measured growth rates for the decay seen here are -3.4×10^{-6} for $\lambda=5\pi R$ and -6.2×10^{-7} for $\lambda=10\pi R$.

Simulations with half-cosine initial conditions for various W and λ provide an indication of the parameter range in which axially stable solutions may lie. For a given W , small-wavelength disturbances should decay, while large-wavelength disturbances should grow. By varying λ , it is possible to approximately locate a cutoff wavelength λ_0 . Such simulations were made, using initial condition (14) with $\alpha_0=0.001\epsilon$. Figure 14 shows the results. Here the lower points (\times symbols) indicate the largest wavelength found to be stable, and the upper points ($+$ symbols) show the small-

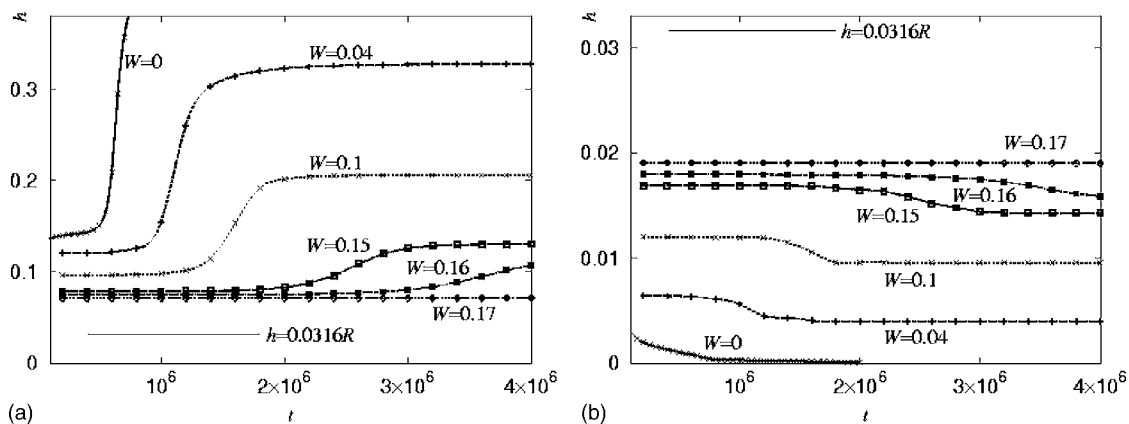


FIG. 12. For the rotating cylinder with $Bo=1$, coating thickness variation is diminished as W increases from 0 to 0.17. Points indicate (a) maximum and (b) minimum values at the given times. The original coating thickness, $h=0.03162R$, is also shown.

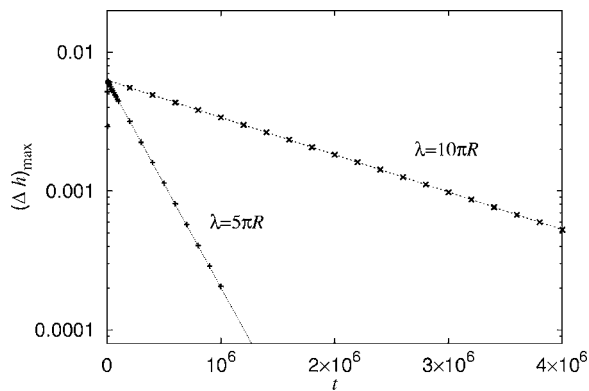


FIG. 13. On a small rotating cylinder with $W=0.2$ and $Bo=1$, $M=0.007$, $\epsilon=0.03162$, axial variations decrease over time. The largest azimuthal variation $(\Delta h)_{\max}$ is defined by Eq. (18). The initial condition is half of a cosine wave along the cylinder length, with the wavelength indicated. Points denote simulation results; straight lines are an exponential fit, from which the (negative) growth rates are found.

est unstable wavelength which was observed. The curve dividing these two sets of points is an estimate of the neutral stability curve, $\lambda_0(W)$. A number of results included here have been confirmed using substantially reduced grid spacing ($n=200$) and time steps.

A number of interesting features are evident. At $W=0$, the coating is strongly influenced by drainage, though the cutoff wavelength appears to be near $2\pi R$. As W increases, so does λ_0 . Near $W=0.15$, λ_0 increases rapidly, exceeding the value $5\pi R$ used in the above simulations when $W \approx 0.175$. The curve was not continued beyond $\lambda=30\pi R$. Disturbances having this wavelength were found to be stable for $0.186 < W < 0.242$, while speeds slower or faster than this lead to the formation of the drop patterns shown in this section. As W is further increased, the cutoff wavelength decreases.

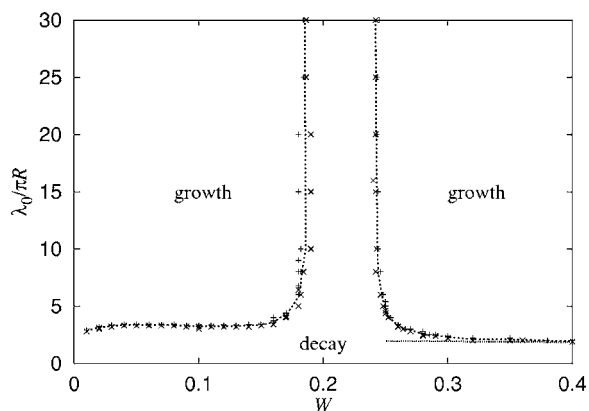


FIG. 14. Stability diagram for a coating on a small rotating cylinder with $Bo=1$, $\epsilon=0.03162$, and $M=0.007$. The horizontal axis shows dimensionless cylinder rotation rate W . The vertical axis shows the wavelength of a small-amplitude sinusoidal variation superposed on an initially uniform coating. Symbols below the line (\times) indicate values for which the disturbance did not grow; symbols above the line ($+$) indicate values for which the disturbance amplitude grew over time. The thin dotted line on the right indicates the cutoff wavelength for the axisymmetric disturbance considered in Sec. III A.

Well above the Moffatt critical speed ($W_c=0.287$), the influence of gravity is weak and the coating is nearly axisymmetric. The theory of Sec. III A should therefore be applicable. As shown in Fig. 14, the cutoff wavelength appears to approach that of an axisymmetric disturbance on a rotating cylinder, given by (10) with $S=W^2Bo$ here.

The above observations suggest that there is a range of speeds for which the axially uniform solution is stable to small perturbations. This is potentially useful for two reasons. First, a coating coated at this speed is unlikely to develop defects. Second, it may be possible to obtain a nearly uniform coating, with (for example) a lower power requirement for rotation than if the speed were raised above the Moffatt critical speed.

The existence of a stable region is not unique to these parameters. With M decreased to 0.005, limited results suggest that the neutral stability curve has a similar shape to that shown in Fig. 14 for $M=0.007$. However, its features are shifted to rotation rates which are $7/5=1.4$ times larger. This is not unexpected. M only appears in the viscous dragging term of (6), where it is multiplied by W , so a decrease in M is compensated for by a corresponding increase in W . The increase in centripetal acceleration caused by larger W appears to have little effect on these parameters. Similarly, when the Bond number was increased to 4 (i.e., the cylinder radius $R=2l_c$), but ϵ and M remained unchanged, a stable region could still be found. In this case, the rapid increase in cutoff wavelength occurred at higher speed, around $W=0.24$. Initial conditions with wavelengths $\lambda=5\pi R$ were found to decay in amplitude for $0.245 < W < 0.265$. For example, the growth rate for $\lambda=5\pi R$ and $W=0.25$ is -1.0×10^{-6} . The stable region extends at least as far as when $Bo=1$, with negative growth rates found for $0.24 < W < 0.26$ when $\lambda=30\pi R$.

We suggest that in these parameter regimes, the coating does not destabilize due to an Rayleigh-Taylor-type instability because cylinder rotation soon carries liquid particles away from the ridge of liquid near the cylinder underside. Furthermore, as rotation rate is increased, the height of this ridge is reduced, discouraging breakup. A detailed explanation for these results awaits further investigation.

While being stable to one wavelength (or even finitely many) does not imply stability to all wavelengths, in this case it is strongly suggestive, since the theory of axisymmetric and Rayleigh-Taylor instabilities (Sec. III A) suggests that the growth rate dependence on wavelength is characterized by a cutoff wavelength, with all shorter wavelengths being stable. Having found one stable wavelength, all shorter wavelengths can be expected to be stable. Conversely, the existence of a single unstable wavelength demonstrates that the axially uniform coating is certainly (linearly) unstable.

Breakup occurs again at higher speeds, though the resulting coating profile is now ringlike, rather than droplike. This is seen in a simulation with $W=0.3$, slightly above the critical speed $W_c=0.287$, starting with same random initial condition as for lower speeds. At first, the coating settles into nearly axially uniform layer, with a shape in close agreement with the two-dimensional solution. Small waves appear at the thickest part of the coating, just below $\theta=0$, by $t=2$

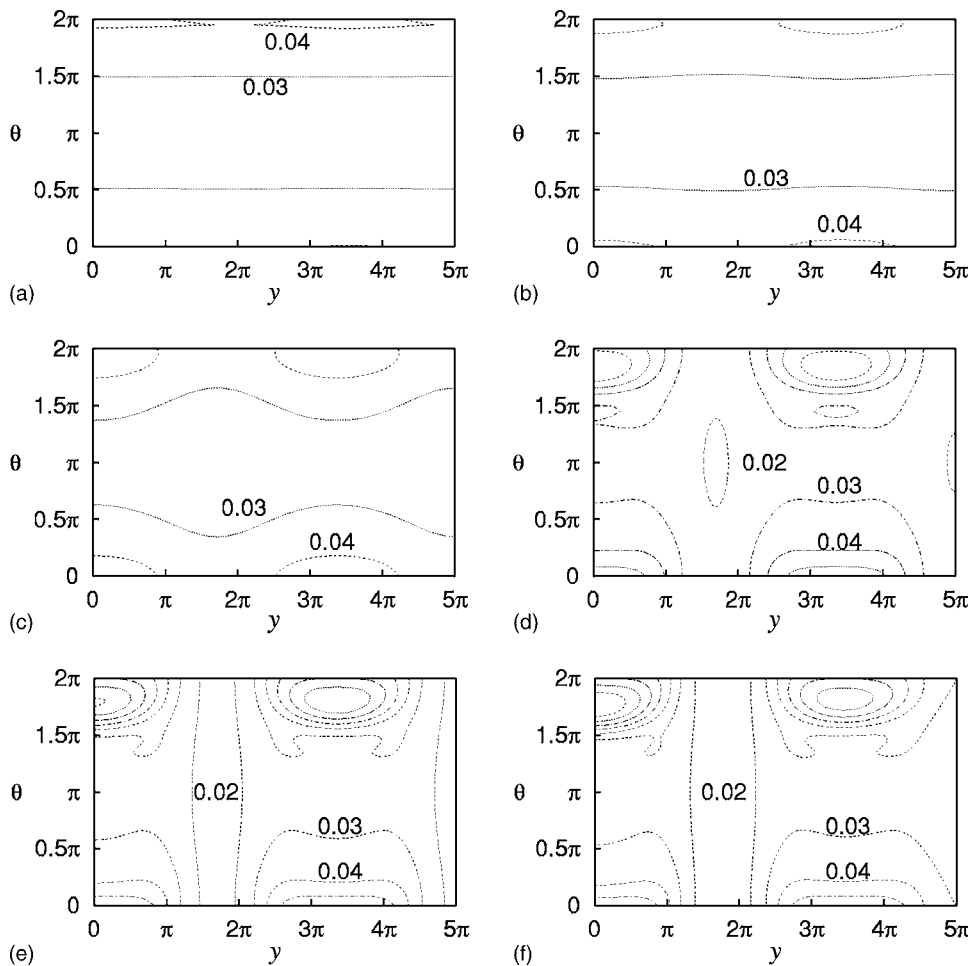


FIG. 15. On a small cylinder rotating above the Moffatt speed, the coating may develop into rings. Here $W=0.3$, while $Bo=1$, $\epsilon=0.03162$, $M=0.007$. Contour plots of coating thickness are shown at (a) $t=2 \times 10^6$; (b) $t=3 \times 10^6$; (c) $t=4 \times 10^6$; (d) $t=5 \times 10^6$; (e) $t=6 \times 10^6$; (f) $t=8 \times 10^6$. The contour interval is 0.01.

$\times 10^6$. These waves slowly grow, appearing as droplets on a ridge of liquid extending along the cylinder axis near $\theta=0$ by $t=4 \times 10^6$ [Figs. 15(a)–15(c)]. As the droplets grow, the ridge begins to break up, until the coating consists of rings of liquid wrapped circumferentially around the cylinder [see Fig. 15(e), $t=6 \times 10^6$], connected by a much thinner coating layer. This arrangement persists for a long time, although, like the drops underneath the stationary cylinder, rings may migrate along the axis. This is seen in Fig. 15(f) where at $t=8 \times 10^6$ the right-hand ring is beginning to drift rightward, later merging with its reflection in the right-hand boundary (not shown). The appearance of these rings is somewhat similar to those observed in experiments.^{1,3,4}

B. Large cylinders: $Bo=100$

We now turn to a larger cylinder, with $R=10l_c$, and viscosity parameter $M=0.007$. Simulations begin with a mean coating thickness $h_0=0.007R$. We presented two-dimensional solutions of (6) with these parameters previously.⁸ For a typical silicone oil (Dow Corning®200 fluid) with $\sigma \approx 21$ dyn/cm and $\rho \approx 0.97$ g/cm³, the capillary length $l_c=0.15$ cm, so these parameters correspond to a cylinder diameter of 3 cm and a coating viscosity $\mu=0.4$ P. The Moffatt critical speed is $\Omega_c=0.36$ s⁻¹ (3.4 rpm), so $W_c=0.0141$. A coating on the stationary cylinder with $Bo=100$ produced drops with a wavelength of between $10.9l_c$ and $12.5l_c$ (see

Sec. III C). We therefore choose a domain length somewhat longer than this, with $L=10\pi l_c=\pi R$, and take $n=400$ and $n_2=200$. In this section, results obtained using (6) are shown; those obtained using (5) were found to be similar and are not shown here.

For a slower speed, $W=0.004$, the coating resembles the stationary case. Starting from the near-random initial condition (17), a bulge of liquid on the upward-moving side grows to form a ridge. As the ridge gains thickness it moves downward, until settling slightly upward of the cylinder underside, with the thickest part located at $\theta \approx 4.79$. Until $t=80\,000$, the coating is well described using the two-dimensional model. Undulations develop along the ridge of liquid, which rapidly grow to form three drops [Figs. 16(a)–16(c)], with a wavelength of $3.3\pi l_c$. This value lies within the range of wavelengths observed for this case when $W=0$. Drop formation is largely complete by $t=120\,000$, corresponding to just over half a revolution of the cylinder. This pattern remains unchanged for at least two further revolutions. The resulting droplet contours are nearly circular [Fig. 16(d)]. Their maximum thickness is about $0.15R$, compared to thicknesses greater than $0.2R$ for the stationary cylinder. The coating profile is shown in perspective form after drop formation is complete in Fig. 17. At this speed, the drops finish slightly upward of the cylinder underside, centered at $\theta=4.74$, having

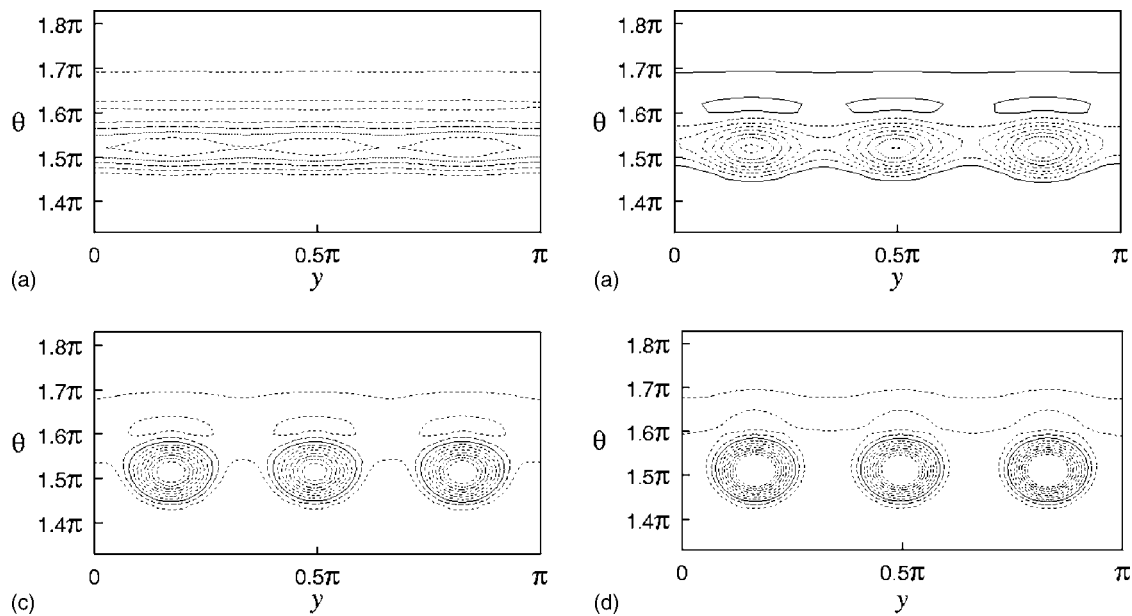


FIG. 16. On a large, slowly rotating, cylinder drops develop. Here $W=0.004$ while $Bo=100$, $\epsilon=0.007$, and $M=0.007$. Contour plots of coating thickness are shown at (a) $t=1 \times 10^5$; (b) $t=1.1 \times 10^5$; (c) $t=1.2 \times 10^5$; (d) $t=2 \times 10^5$. The contour interval is 0.01.

formed only slightly higher. A small, undulating ridge is visible above the drops in Fig. 16(d), hinting at the possibility of secondary drops forming there.

In previous work, Hosoi and Mahadevan²² found that the wavelength of the axial instability they saw in a rimming geometry was proportional to the width of the liquid ridge, and satisfied $\lambda \sim \sigma^{1/3}$. This scaling results from the dominant forces in the ridge, namely, capillarity and viscosity.^{21,34} We measured the ridge width w for a range of Bond numbers between 2 and 500 (with ϵ , M , and W fixed), using the two-dimensional form of (6), finding that it indeed varies like $Bo^{-1/3}$. We define the width w to be the angle between the locations of the thickness minima which occur on either side of the ridge. As Bond number is increased, the width reduces and the preferred wavelength of the instability decreases. For large Bo , our limited numerical evidence suggests that the wavelength appears to reduce with w . Of course for small Bo , the curvature of the cylinder becomes important, and the instability wavelength approaches a constant multiple of the cylinder radius.

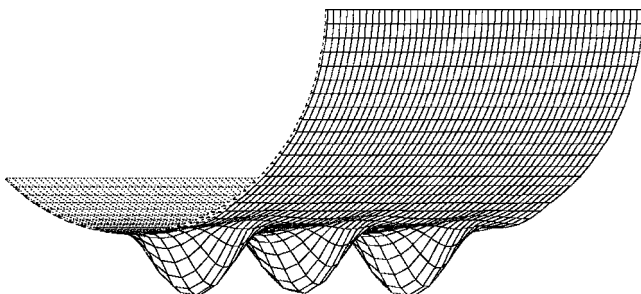


FIG. 17. Drops on the underside of a large, slowly rotating cylinder. Perspective view of the coating shown in Fig. 16 at $t=2 \times 10^5$. Coating thickness has been exaggerated two times.

Not far below the critical speed, with $W=0.012$, the coating evolves somewhat differently, forming long fingers. The initial ridge of liquid forms much higher (at $\theta \approx 5.5$), and is thinner than for the slower cylinder, with a maximum thickness of about $0.01R$. The breakup into droplets is much slower than when $W=0.004$. Appreciable droplets do not appear until about $t=4 \times 10^5$ [Figs. 18(a) and 18(b)]. By $t=10^6$, $3\frac{1}{2}$ drops have formed [Figs. 18(c) and 18(d)]. The point of maximum coating thickness at this time is located at $\theta=5.35$, as the drops drain downward from the initial ridge. Later, the leftmost complete drop merges with the half drop at the boundary to form a more massive single drop [Figs. 18(e) and 18(f)] which settles further down the cylinder than the other two drops.

C. Summary

This section has shown how the three-dimensional model can be used to simulate coatings on cylinders of different diameters for a number of rotation rates. An initial coating which is nearly uniform evolves in an axially uniform manner at first, forming a ridge. For slowly rotating cylinders, this ridge is relatively large, and is close to the underside of the cylinder, similar to the stationary case. At high rotation rates, the initial liquid ridge is thinner and broader, and situated well up the front of the cylinder.

For small cylinders, the ridge eventually breaks into drops, except when W is in a range of speeds slightly less than W_c . These drops are large compared to the cylinder radius. As speed is increased the drop shapes alter from being circular to elongated. At higher speed, there is a transition from ridge-like to ring-like appearance, with rings of liquid wrapped around the cylinder. In the $Bo=1$ case con-

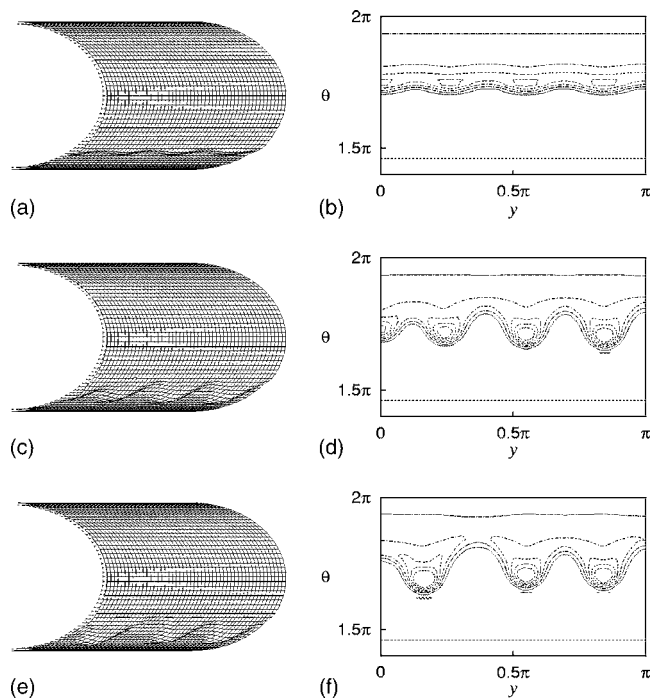


FIG. 18. On a large, faster-rotating cylinder, drops form on the upward-moving cylinder surface. Simulation parameters are the same as Fig. 16, except that W is increased to 0.012. The coating is shown at (a) and (b) $t = 0.4 \times 10^6$; (c) and (d) $t = 1.0 \times 10^6$; (e) and (f) $t = 1.5 \times 10^6$. Coating profiles in (a), (c), and (e) have been exaggerated five times. The contour interval in (b), (d), and (f) is 0.002.

sidered here, it appears there is a range of rotation rates in which the axially uniform coating has no tendency to break up.

On the larger cylinders, with $Bo = 100$, the drops formed are small compared to the radius. At low speeds, drops are located at the bottom of the cylinder, but as speed is increased they form further up the upward-moving side. The undershoot below the liquid ridge requires relatively fine resolution. In the present numerical model, with uniform grid spacing, this makes simulation expensive. Some form of nonuniform, or adaptive, meshing would be helpful here.

V. EXPERIMENTAL COMPARISON

To verify some of the phenomena seen in simulations, and in particular to study the breakup into droplets, a number of simple experiments were performed. Figure 19 shows a smooth steel cylinder, designed as a roller in a pilot coating machine. It could be rotated using a compressed-air-driven motor capable of rotating the cylinder at speeds in excess of 60 rpm ($2\pi \text{ s}^{-1}$). This was coated by a silicone oil (polydimethylsiloxane) provided by Dow Corning. The properties of the cylinder and oil are given in Table I.

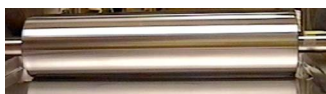


FIG. 19. The steel roller used for experiments. The tray used for coating the cylinder with silicone oil is underneath.

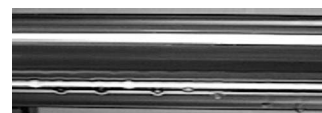


FIG. 20. Formation of a row of droplets. The cylinder is seen from the front, with the visible part moving upwards.

The coating was prepared by holding a shallow tray of silicone oil just below the underside of the roller. With the cylinder rotating at constant speed, the tray was raised so that oil was drawn up to coat the entire surface. The tray was then quickly lowered, leaving a large amount of liquid on the cylinder. Sometimes, some excess liquid would immediately drip off for a short time. The resulting coating layer appeared not to vary along the cylinder axis. The coating mass, and in turn the volume and the average film thickness, were determined by measuring the mass change of silicone oil in the tray due to the application of the coating. Rotation rates were determined by measuring the time taken for a fixed number of revolutions with a stopwatch. Often there was appreciable variation in the rotation rate, which is attributed to a variation in the compressed air supply. Although the alignment of the cylinder axis was checked with a spirit level, often one end was slightly lower than the other. This caused a slow drainage along the axis, and a thicker average coating at one end.

In the experiment reported here, the roller was loaded with liquid at a relatively high speed ($\sim 2 \text{ s}^{-1}$), and gradually slowed over several minutes. With the rotation rate at about 1.03 s^{-1} a row of drops formed from a ridge of liquid at the front of the cylinder, near the $\theta = 0$ position. Figure 20 shows nine such drops. The two rightmost drops, which have drained somewhat further, formed a few seconds before the others. The spacing of these drops varied from 1.6 cm to 3.4 cm, with an average spacing of 2.3 cm.

Within about 90 s the drops shown here grew into fingers, which drain downward to settle near the cylinder underside. Figure 23 shows the coating layer 5 min after the appearance of the drops, from below and to one side. The rotation rate had decreased slightly to about 0.91 s^{-1} . In some experiments, so much liquid sometimes accumulated in a drop that it broke away, removing liquid from the coating. The part of the drop remaining on the cylinder then quickly “rebounded” to its original position, slightly forward of the bottom of the cylinder. This has already occurred for the rightmost drop in Fig. 23. When the cylinder was stopped, all the liquid on the cylinder drained, and about 19 drops formed along the underside, corresponding to a somewhat closer average spacing of about 1.5 cm.

The above experiment can be compared with a simulation using our model. The simulation parameters for the experimental conditions are shown in Table II. The volume of liquid in this case was found to be 18.5 cm^3 , corresponding to a mean thickness of 0.0313 cm, so the thickness parameter $\epsilon = 0.009$. The capillary length was $l_c = 0.15 \text{ cm}$, so $R = 22.4l_c$ and $Bo \approx 500$. Based on a constant rotation rate of $\Omega = 0.95 \text{ s}^{-1}$, the dimensionless rotation rate $W = 0.056$ was used. The critical value of Ω for Moffatt-type solutions for

TABLE II. Dimensionless parameters for comparison with experiment.

Property, symbol	Value
Thickness, ϵ	0.009
Bond number, Bo	500
Viscosity parameter, M	0.0026
Rotation parameter, W	0.056

these parameters, given by (2), is $\Omega_c = 1.06 \text{ s}^{-1}$, slightly faster than the value used here. The simulation, using (6), began with a nearly uniform layer of thickness $0.009R$, with applied noise of 1% of the thickness. The model cylinder is somewhat shorter (length πR) than in the experiment, with length $8.2R$. We have used $n=400$ and $n_2=200$ here.

In our simulations, a bulge of liquid quickly forms on the upward-moving side, just below $\theta=0$. This bulge increases in thickness, forming a ridge, with little axial variation evident. After some time, undulations develop along the liquid ridge, which rapidly grow to form drops by $t=60\,000$. Contour plots of the simulated coating (Fig. 21) illustrate this clearly. These drain down the front of the cylinder as long fingers. In the simulation the spacing between drops varies from $0.36R$ to $0.49R$, with an average spacing of $0.44R$. This is somewhat shorter than the spacing seen in Fig. 20. The free surface profile at $t=80\,000$ (1.9 revolutions) is shown in Fig. 22. Computer rendering is used to view the

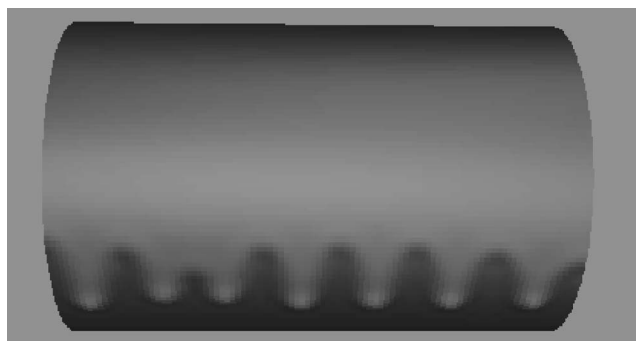


FIG. 22. Result of the same numerical simulation as in Fig. 21, showing the formation of a row of droplets. This may be compared with the experimental result shown in Fig. 20. The cylinder is seen from the front, with the visible part moving upwards, at $t=80\,000$.

coating from the front, shading the coating based on its thickness. Late in the simulation, the second and third fingers from the left in Fig. 22 merge, forming a larger finger. Figure 24 shows the computed free surface later, at $t=180\,000$ (4.2 revolutions), viewed from an angle similar to that of Fig. 23, below and to one side of the cylinder. The elongated shape of the droplets, and their position slightly toward the upward-moving side of the cylinder, qualitatively agrees with the experimental results.

Liquid accumulates near the bottom of the cylinder at $\theta=3\pi/2$, and the thickness of the drops there gradually in-

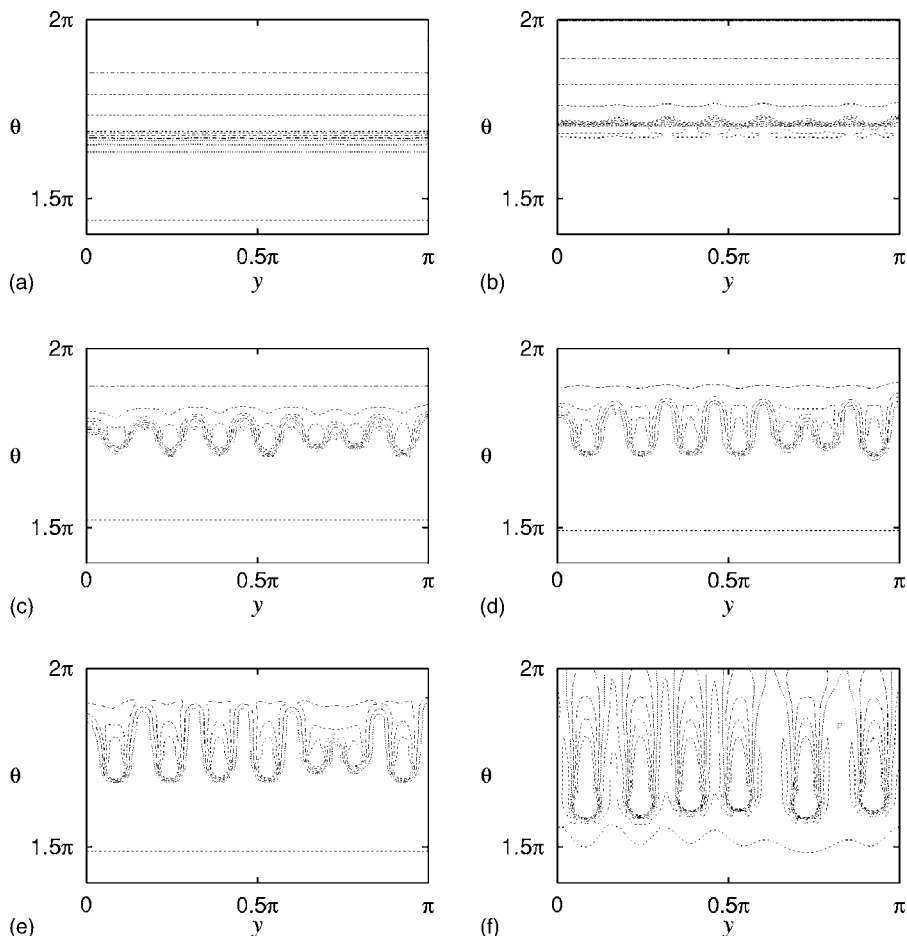


FIG. 21. Breakup into droplets on a large rotating cylinder, using the three-dimensional numerical model. Parameters correspond to the experiment, and are given in Table II. Contour plots of coating thickness are shown at (a) $t=2 \times 10^5$; (b) $t=4 \times 10^5$; (c) $t=6 \times 10^5$; (d) $t=8 \times 10^5$; (e) $t=10 \times 10^5$; (f) $t=20 \times 10^5$. The contour interval is 0.002, though contours are not shown for thicknesses exceeding 0.018.



FIG. 23. Over time the droplets in the experiment shown in Fig. 20 accumulate the liquid and grow to form long fingers. The cylinder is seen from below the horizontal, and to one side.

increases over time. Eventually our model and numerical simulations fail as a result of the excessive changes in thickness near the edge of the drop. To reach the point shown in Fig. 24 required less than an hour on a 1 GHz Pentium-class personal computer.

In some experiments, isolated fingers would appear, without the sequence of ridge formation and breakup into many drops presented above. These are attributed to local variations in the thickness of the initial coating, which arise from the tray used to load the cylinder not being either perfectly flat or held perfectly level. Such a finger is shown in Fig. 25. To study these fingers, a simulation was performed using a much narrower portion of the cylinder. Simulations begun from half-cosine initial conditions indicated that the cutoff wavelength for disturbances to grow was between $0.35R$ and $0.38R$ for the parameters in Table II. With $L = \pi R/10$ ($n_2=20$), a half-cosine variation with a wavelength of $\pi R/5$ was imposed in the axial direction. This grew to produce one-half of a finger, shown in Fig. 26, which drains down the front of the cylinder. Its tail extends into the upper half of the cylinder at later times, though this is cut off in the figures. The general appearance of the finger is similar to that of Fig. 25, and also somewhat like that shown in simulations by Schwartz³⁶ for a drop draining on a vertical wall. There is

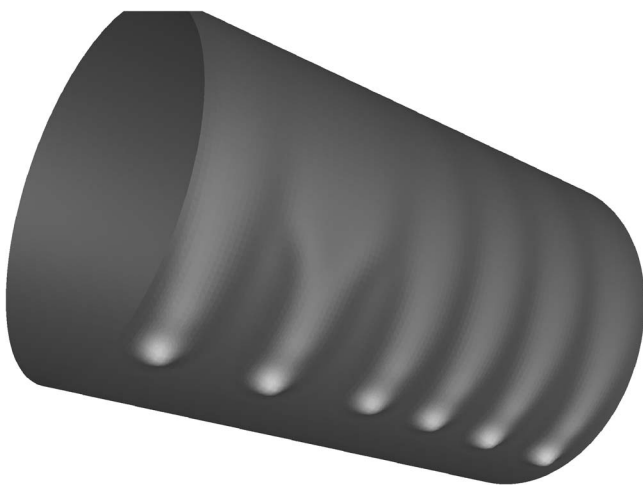


FIG. 24. Computed free surface for the simulation shown in Fig. 21. Fingers drain toward the cylinder underside at $t=180\,000$. Compare Fig. 23.



FIG. 25. An isolated finger after it has reached the underside of the cylinder.

a relatively thick region behind the main drop. The position of maximum coating thickness, which is at the head of the finger, advances at nearly constant speed, until reaching the bottom of the cylinder.

VI. DISCUSSION

This work has presented simulations of coating flow on a rotating cylinder, extending previous work in two complementary ways. First, we used a three-dimensional coating evolution equation which adequately includes the effects of rotation, surface tension, centripetal acceleration, gravity, and axial variation, for a rotating cylinder, in a parameter range where all these effects are significant. The numerical results here are an extension of our earlier work⁸ in two dimensions to include axial variation. This work can also be viewed as the extension of work by Weidner *et al.*¹² for stationary cylinders to rotating cylinders. Our experimental results have confirmed the general features of the simulations.

A numerical method was developed for obtaining solutions using the model. This was implemented in three dimensions using an alternating direction implicit (ADI) finite-difference method. The numerical method was verified, with gravity excluded, by comparing the observed growth rate of an axisymmetric sinusoidal disturbance with a linearized theory. The coating is unstable to this disturbance, and the coating breaks up into rings wrapped around the cylinder. With gravity included, model predictions were compared with existing results for a stationary cylinder.¹² In this case, the liquid drains under the influence of gravity, forming a ridge beneath the cylinder, which breaks up to form pendant drops. As is well known,³¹ the spacing of these drops is strongly influenced by the cylinder size relative to the coating capillary length. For small cylinders, the drop spacing scales with the cylinder radius. For large cylinders, the Rayleigh-Taylor instability causes the drops to have a wavelength determined by the coating capillary length.

Using this model we are able to perform realistic numerical simulations of the three-dimensional coating, includ-

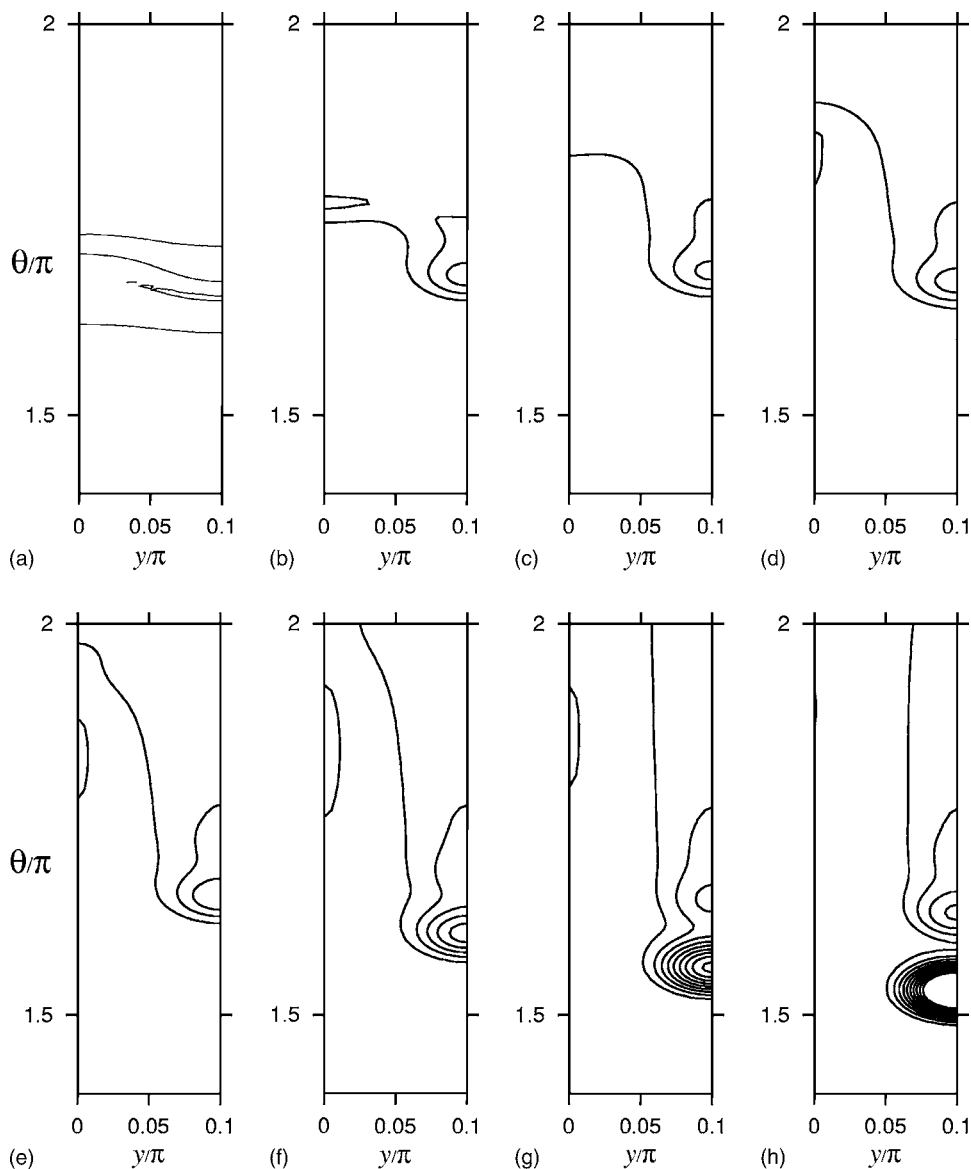


FIG. 26. Development of a finger on a rotating cylinder, using the three-dimensional numerical model. The finger is produced using a sinusoidal initial condition with axial wavelength $\pi/5$. Contour plots of coating thickness are shown at (a) $t=2 \times 10^5$; (b) $t=4 \times 10^5$; (c) $t=6 \times 10^5$; (d) $t=8 \times 10^5$; (e) $t=1.0 \times 10^6$; (f) $t=1.5 \times 10^6$; (g) $t=2.0 \times 10^6$; (h) $t=2.5 \times 10^6$. The contour interval is 0.01. Coating parameters are the same as in Fig. 21.

ing reproducing the fingering seen in an experiment. In general a coating on a rotating cylinder displays the same initial behavior regardless of cylinder size or rotation rate. A nearly uniform initial coating first adopts a profile which is axially uniform, and so it is well described by the two-dimensional model. A ridge of liquid forms on the upward-moving side of the cylinder. For most of the parameter ranges considered, an axial instability develops on this ridge, causing it to break up. The simple experiments presented here confirm that an apparently axially uniform layer may develop a nonuniform surface over time. The mechanism responsible for the breakup is presumably surface tension, since neither gravitational nor rotational forces act in the axial direction.

Depending on the particular parameters, this leads to the formation of one of several possible configurations. At low speeds, the coating on both large and small cylinders settles into a steady state, with drops of liquid near the underside. These drops become elongated as the cylinder speed increases. At somewhat higher speeds, rings may form on a small cylinder, as observed previously. For larger cylinders,

ridges form well up the upward-moving side of the cylinder and break up to form long fingers which drain to the cylinder underside.

We report observations of fingers in both numerical simulations and experiments. For large cylinders, the numerical method is able to qualitatively reproduce experimental observations of fingering. A simulation using the experimental parameters produced fingers showing reasonable agreement with the results of our experiment. These fingers are somewhat similar to the features seen in rimming flows of liquids^{20,22} and granular materials.³⁷ Fingering appears to be a result of the buildup of liquid on the upward-moving side, but the precise mechanism for instability remains unclear. The model here will allow further investigation of such behavior.

Because rotation continually carries the liquid over the entire coating, there is a nonzero minimum coating thickness, even after breakup has occurred. This occurs on the downward-moving side close to $\theta=\pi$, as expected from Moffatt's theory. In contrast, on a stationary cylinder all liq-

uid will eventually drain from the upper parts of the cylinder.

For a certain parameter range, we have obtained numerical evidence suggesting that the liquid ridge is not unstable to axial perturbations. For a small ($Bo=1$) rotating cylinder, there appears to be a stable speed window below the Moffatt speed, in which the coating does not break up axially into droplets or rings. This is a surprising result, given that the coating might be expected to remain unstable to an axisymmetric “sausage-type” instability. This may be because in this parameter range the cutoff wavelength for axial instability becomes larger than could be studied here, or because the axially uniform profile is in fact stable. This stable region appears to persist for somewhat larger cylinders. A useful task would be identification of the fastest-growing wavelength of the transverse instability observed using the numerical method and its growth rate. The latter is expected to decrease as the stable region is approached. Further analytical and numerical investigation is needed to shed light on this question. The existence of a stable speed window might be confirmed by careful experiments.

Our three-dimensional simulations have not yet revealed a systematic variation in the preferred wavelength as the rotation rate is increased. The experimental evidence shows that the spacing in the drippers seen in Fig. 23 is somewhat larger than the spacing of the drips which form on the cylinder underside when the cylinder is stopped and the liquid drains off. At high speeds where centrifugal acceleration is significant, the theory of Sec. III A suggests a shorter wavelength for instability. This apparent discrepancy is perhaps a result of finite-length effects, due to the relatively short cylinder lengths used here.

An important refinement of the numerical method would be the incorporation of full curvature and correct mass conservation, including the higher-order terms in (4) which were neglected in the current work. With the present method, the liquid accumulates in drops near the bottom of the cylinder, and the coating thickness gradually increases over time. Eventually simulations fail as a result of the excessive changes in thickness in this area. Such a scheme has been implemented for the stationary cylinder by Weidner *et al.*¹² This would prevent the coating from growing to nonphysical size and allow treatment of the maximum load problem.

For small Bond numbers, resolving features on the order of the capillary length l_c requires many grid points. The three-dimensional numerical method currently used requires that the dimensionless grid spacings $\Delta\theta$ and Δy are equal. Removing this restriction would allow more efficient modeling of long or short stretches of cylinder, while ensuring adequate resolution.

One of the original goals of this work was to improve understanding of the maximum amount of coating which can be supported on a rotating cylinder. The present work, while not directly addressing this issue, highlights the importance of accurate three-dimensional modeling of drop formation and fingering. Fingers drain and large drops accumulate the liquid, before dripping off, removing the liquid from the cylinder. These lower the amount of liquid which can be held below that which would be expected for an axially uniform coating. Any complete answer to the maximum load question

must include the effects of these processes. Conversely, in coating operations where a thin and uniform coating is desired, any axial instability is unwanted. In either case, a better understanding of the development of such instabilities will be important for progress.

ACKNOWLEDGMENTS

This work was supported by ICI, the State of Delaware, and the NASA Microgravity Program.

APPENDIX A: COATING FLOW MODEL

Here we summarize the derivation⁸ of the lubrication equation (4). The liquid velocity is written as $\mathbf{u}(r, \theta, y, t) = w\mathbf{e}_r + (r\Omega + u)\mathbf{e}_\theta + v\mathbf{e}_y$ in cylindrical coordinates (r, θ, y) where \mathbf{e}_r , \mathbf{e}_θ , and \mathbf{e}_y are coordinate unit vectors which are fixed (independent of time) in a nonrotating frame. The continuity and momentum conservation equations are

$$\nabla \cdot \mathbf{u} = \frac{1}{r} \frac{\partial}{\partial r}(rw) + \frac{1}{r} \frac{\partial u}{\partial \theta} + \frac{\partial v}{\partial y} = 0, \quad (\text{A1})$$

$$\left[\frac{\partial w}{\partial t} + w \frac{\partial w}{\partial r} + \frac{u}{r} \frac{\partial w}{\partial \theta} + v \frac{\partial w}{\partial y} - \frac{u^2}{r} \right] + \Omega \left(\frac{\partial w}{\partial \theta} - 2u \right) - r\Omega^2 = -\frac{1}{\rho} \frac{\partial p}{\partial r} + \frac{\mu}{\rho} \left\{ \nabla^2 w - \frac{w}{r^2} - \frac{2}{r^2} \frac{\partial u}{\partial \theta} \right\} - g \sin \theta, \quad (\text{A2})$$

$$\left[\frac{\partial u}{\partial t} + w \frac{\partial u}{\partial r} + \frac{u}{r} \frac{\partial u}{\partial \theta} + v \frac{\partial u}{\partial y} + \frac{uw}{r} \right] + \Omega \left(\frac{\partial u}{\partial \theta} + 2w \right) = -\frac{1}{\rho r} \frac{\partial p}{\partial \theta} + \frac{\mu}{\rho} \left\{ \nabla^2 u - \frac{u}{r^2} + \frac{2}{r^2} \frac{\partial w}{\partial \theta} \right\} - g \cos \theta, \quad (\text{A3})$$

$$\left[\frac{\partial v}{\partial t} + w \frac{\partial v}{\partial r} + \frac{u}{r} \frac{\partial v}{\partial \theta} + v \frac{\partial v}{\partial y} \right] + \Omega \frac{\partial v}{\partial \theta} = -\frac{1}{\rho} \frac{\partial p}{\partial y} + \frac{\mu}{\rho} \{ \nabla^2 v \}, \quad (\text{A4})$$

where p is the liquid pressure. Here

$$\nabla^2 \phi = \frac{1}{r} \frac{\partial}{\partial r} \left(r \frac{\partial \phi}{\partial r} \right) + \frac{1}{r^2} \frac{\partial^2 \phi}{\partial \theta^2} + \frac{\partial^2 \phi}{\partial y^2}.$$

These equations are to be solved in the interval $0 < z < h(\theta, y, t)$, where $z = r - R$, subject to the following boundary conditions.

(1) At the moving wall a no-slip boundary condition is applied: $u = v = w = 0$ at $z = 0$.

(2) At the free surface $z = h$, the shear stresses are zero, and normal stress arises from pressure and surface tension effects, so

$$\mathbf{n} \cdot \boldsymbol{\tau} \cdot \mathbf{t}_\alpha = 0 \quad \text{for } \alpha = \{1, 2\},$$

$$-p + \mu(\mathbf{n} \cdot \boldsymbol{\tau} \cdot \mathbf{n}) = -\sigma \kappa.$$

Here $\boldsymbol{\tau} = (\nabla \mathbf{u} + \nabla \mathbf{u}^T)/2$ is the fluid rate-of-strain tensor, and \mathbf{n} and \mathbf{t}_α are unit vectors normal and tangential to the free surface, respectively. κ is the free surface curvature.

(3) At the free surface $F(\theta, y, z, t) = z - h(\theta, y, t) = 0$, $DF/Dt = 0$, where D/Dt is the usual material derivative. This boundary condition is used to obtain the evolution equation for the film thickness.

Equations (A1)–(A4), together with the above boundary conditions, form a complete statement of the general problem. In our earlier work,⁸ a perturbation expansion in the small parameter $\epsilon = H/R \ll 1$ is carried out, where H is the characteristic film thickness. This requires scaling the fluid velocity components along the substrate with $\rho g H^2 / \mu$, pressure with $\rho g H$, and time with $\mu R / \rho g H^2$.

To leading order the variable part of the pressure (in physical variables) is

$$p = -\sigma \left(\frac{h}{R^2} + \nabla^2 h \right) + \rho [(R+z)\Omega^2 - g \sin \theta] [z - h].$$

Here the nonlinear expression for the free surface curvature has been approximated by a linearized expression. This is appropriate when $h \ll R$, i.e., $\epsilon \ll 1$.

The components of fluid velocity along the substrate, in the azimuthal and axial directions respectively, are

$$u = -\frac{\partial}{\partial \theta} \left\{ \sigma (h + \nabla^2 h) + [R\Omega^2 - \rho g \sin \theta] h \right\} \left[\frac{z^2}{2} - hz \right] \\ - \cos \theta \left[\frac{z^2}{2} - hz + \frac{z^3}{3} - hz^2 + \frac{3h^2 z}{2} \right] + (R+z)\Omega, \\ v = -\frac{\partial}{\partial y} \left\{ \sigma (h + \nabla^2 h) + [R\Omega^2 - \rho g \sin \theta] h \right\} \left[\frac{z^2}{2} - hz \right].$$

Integrating the fluid velocity across the film thickness leads to an evolution equation for the coating thickness, $h(\theta, y, t)$. This is Eq. (3).

APPENDIX B: THREE-DIMENSIONAL NUMERICAL SCHEME

To solve (6) numerically, a finite-difference method is used. The coating thickness h at $(\theta_i, y_j) = (i\Delta, j\Delta)$ is approximated by $h_{i,j}^{(k)}$ at time level $t^{(k)}$. Equation (6) is solved using an ADI scheme similar to that described by Yanenko³⁸ for solving equations of biharmonic type arising in the theory of elasticity. The fourth-order derivatives are treated implicitly, while other quantities are treated explicitly. This avoids the restrictive small time step requirement for the stability of a fully explicit method.

At the end surfaces $y=0$ and $y=L$, zero flux boundary conditions are imposed:

$$\frac{\partial h}{\partial y} = \frac{\partial^3 h}{\partial y^3} = 0 \quad \text{at } y = 0, L.$$

In the θ direction, the coating is required to be periodic, i.e., $h(\theta + 2\pi, y, t) = h(\theta, y, t)$. References to $i, i \pm 1, i \pm 2$ in the first subscript of $h_{i,j}^{(k)}$ should be understood to be modulo n in the following description.

Each full time step, from the k th to the $(k+1)$ th time level, is divided into two half-time steps, with fictitious intermediate values $h_{i,j}^{(k+1/2)}$ computed at time $t = (t^{(k)} + t^{(k+1)})/2$. It is useful to define the finite difference operators

$$\Delta_x f_{i,j} = (f_{i+1/2,j} - f_{i-1/2,j})/\Delta,$$

$$\Delta_y f_{i,j} = (f_{i,j+1/2} - f_{i,j-1/2})/\Delta,$$

$$\Delta_\theta^2 f_{i,j} = (f_{i+1,j} - 2f_{i,j} + f_{i-1,j})/\Delta^2,$$

$$\Delta_y^2 f_{i,j} = (f_{i,j+1} - 2f_{i,j} + f_{i,j-1})/\Delta^2.$$

In the first half time step, the highest order θ derivative is treated implicitly, while the viscous dragging term is handled using a time-centered difference:

$$c_{i,j}^{(k)} \frac{h_{i,j}^{(k+1/2)} - h_{i,j}^{(k)}}{\Delta t} = -\frac{1}{3\text{Bo}\Delta} \left\{ (h_{i+1/2,j}^{(k)})^3 (A_{i+1/2,j}^{(k)} + B_{i+1/2,j}^{(k+1/2)} + \Delta_\theta h_{i+1/2,j}^{(k)}) - (h_{i-1/2,j}^{(k)})^3 (A_{i-1/2,j}^{(k)} + B_{i-1/2,j}^{(k+1/2)} + \Delta_\theta h_{i-1/2,j}^{(k)}) \right\} \\ + \frac{(h_{i+1/2,j}^{(k)})^3 C_{i+1/2,j}^{(k)} - (h_{i-1/2,j}^{(k)})^3 C_{i-1/2,j}^{(k)}}{3\Delta} + f \frac{(h_{i+1/2,j}^{(k)})^4 \cos \theta_{i+1/2} - (h_{i-1/2,j}^{(k)})^4 \cos \theta_{i-1/2}}{2\Delta} \\ - MW \frac{(h_{i+1,j}^{(k)} + h_{i+1,j}^{(k+1/2)}) - (h_{i-1,j}^{(k)} + h_{i-1,j}^{(k+1/2)}) + f[(h_{i+1,j}^{(k)})^2 - (h_{i-1,j}^{(k)})^2]}{4\Delta},$$

where $\Delta t = t^{(k+1)} - t^{(k)}$ and

$$A_{i+1/2,j}^{(k)} = (\Delta_y^2 h_{i+1,j}^{(k)} - \Delta_y^2 h_{i,j}^{(k)})/\Delta,$$

$$B_{i+1/2,j}^{(k)} = (\Delta_\theta^2 h_{i+1,j}^{(k)} - \Delta_\theta^2 h_{i,j}^{(k)})/\Delta,$$

$$C_{i+1/2,j}^{(k)} = [W^2 - \sin \theta_{i+1/2}] \Delta_\theta h_{i+1/2,j}^{(k)} + \cos \theta_{i+1/2}.$$

For each value of $j \in \{0, \dots, n_2\}$, a periodic pentadiagonal system of n linear equations are solved for the $h_{i,j}^{(k+1/2)}$, using a variant of the standard method for a pentadiagonal system.³⁹ Here $c_{i,j}^{(k)} = 1 + f h_{i,j}^{(k)}$ reflects the cylindrical coordinate system used. In solving (5) we set $f=1$, while for (6) $f=0$.

In the second half-time step, the highest order y derivative is treated implicitly:

$$c_{i,j}^{(k+1/2)} \frac{h_{i,j}^{(k+1)} - h_{i,j}^{(k+1/2)}}{\Delta t} = - \frac{1}{3B_0\Delta} \{ (h_{i,j+1/2}^{(k+1/2)})^3 (D_{i,j+1/2}^{(k+1/2)} + E_{i,j+1/2}^{(k+1)} + \Delta_y h_{i,j+1/2}^{(k+1/2)}) - (h_{i,j-1/2}^{(k+1/2)})^3 (D_{i,j-1/2}^{(k+1/2)} + E_{i,j-1/2}^{(k+1)} + \Delta_y h_{i-1/2,j}^{(k+1/2)}) \} \\ + \frac{(h_{i,j+1/2}^{(k)})^3 F_{i,j+1/2}^{(k)} - (h_{i,j-1/2}^{(k)})^3 F_{i,j-1/2}^{(k)}}{3\Delta},$$

where

$$D_{i+1/2,j}^{(k)} = (\Delta^2 \theta h_{i,j+1}^{(k)} - \Delta^2 \theta h_{i,j}^{(k)}) / \Delta,$$

$$E_{i+1/2,j}^{(k)} = (\Delta_y^2 h_{i,j+1}^{(k)} - \Delta_y^2 h_{i,j}^{(k)}) / \Delta,$$

$$F_{i,j+1/2}^{(k)} = [W^2 - \sin \theta_i] \Delta_y h_{i,j+1/2}^{(k)}.$$

To obtain the values of $h_{i,j}^{(k+1)}$ at the end of this half-time step for each value of $i \in \{0, \dots, n\}$, a pentadiagonal system of $(n_2 + 1)$ equations must be solved for the $h_{i,j}^{(k+1)}$.

¹H. K. Moffatt, "Behaviour of a viscous film on the outer surface of a rotating cylinder," *J. Mec.* **16**, 651 (1977).

²J. P. Kovac and R. T. Balmer, "Experimental studies of external hydrocysts," *J. Fluids Eng.* **102**, 226 (1980).

³D. D. Joseph and L. Preziosi, "Stability of rigid motions and coating films in bicomponent flows of immiscible liquids," *J. Fluid Mech.* **185**, 323 (1987).

⁴L. Preziosi and D. D. Joseph, "The run-off condition for coating and rimming flows," *J. Fluid Mech.* **187**, 99 (1988).

⁵M. A. Kelmanson, "Theoretical and experimental analyses of the maximum-supportable fluid load on a rotating cylinder," *J. Eng. Math.* **29**, 271 (1995).

⁶C.-S. Yih, "Instability of a rotating liquid film with a free surface," *Proc. R. Soc. London, Ser. A* **258**, 63 (1960).

⁷S. B. G. O'Brien, "A model for the coating of cylindrical light bulbs," in *Progress in Industrial Mathematics at ECMI 98*, edited by L. Arkerud, J. Bergh, P. Brenner, and R. Pettersson (Teubner, Stuttgart, 1999), pp. 45–54.

⁸P. L. Evans, L. W. Schwartz, and R. V. Roy, "Steady and unsteady solutions for coating flow on a rotating horizontal cylinder: Two-dimensional theoretical and numerical modeling," *Phys. Fluids* **16**, 2742 (2004).

⁹E. B. Hansen and M. A. Kelmanson, "Steady, viscous, free-surface flow on a rotating cylinder," *J. Fluid Mech.* **272**, 91 (1994).

¹⁰R. C. Peterson, P. K. Jimack, and M. A. Kelmanson, "On the stability of viscous free-surface flow supported by a rotating cylinder," *Proc. R. Soc. London, Ser. A* **457**, 1427 (2001).

¹¹S. L. Goren, "The instability of an annular thread of fluid," *J. Fluid Mech.* **12**, 309 (1962).

¹²D. E. Weidner, L. W. Schwartz, and M. H. Eres, "Simulation of coating layer evolution and drop formation on horizontal cylinders," *J. Colloid Interface Sci.* **187**, 243 (1997).

¹³E. D. Cohen and E. B. Gutoff, *Modern Coating and Drying Technology*, Interfacial Engineering Series, Vol. 1 (VCH, New York, 1992).

¹⁴S. D. R. Wilson and J. Williams, "The flow of a liquid film on the inside of a rotating cylinder, and some related problems," *Phys. Fluids* **9**, 2184 (1997).

¹⁵S. B. G. O'Brien and E. G. Gath, "The location of a shock in rimming flow," *Phys. Fluids* **10**, 1040 (1998).

¹⁶J. Ashmore, A. E. Hosoi, and H. A. Stone, "The effect of surface tension on rimming flows in a partially filled rotating cylinder," *J. Fluid Mech.*

479, 65 (2003).

¹⁷J. A. Dieber and R. L. Cerro, "Viscous flow with a free surface inside a horizontal rotating drum," *Ind. Eng. Chem. Fundam.* **15**, 102 (1976).

¹⁸M. Ehmman and J. Siekmann, "Numerical study of the oscillations of axially excited liquid annuli with rotational symmetry enclosed in revolving circular cylindrical containers," *J. Fluid Mech.* **297**, 215 (1995).

¹⁹H. L. Reed, "Gallery of fluid motion," *Phys. Fluids* **8**, S1 (1996); **8**, S10 (1996).

²⁰S. T. Thoroddsen and L. Mahadevan, "Experimental study of coating flows in a partially-filled horizontally rotating cylinder," *Exp. Fluids* **23**, 1 (1997).

²¹S. M. Troian, E. Herbolzheimer, S. A. Safran, and J. F. Joanny, "Fingering instabilities of driven spreading films," *Europhys. Lett.* **10**, 25 (1989).

²²A. E. Hosoi and L. Mahadevan, "Axial instability of a free-surface front in a partially filled horizontal rotating cylinder," *Phys. Fluids* **11**, 97 (1999).

²³F. Melo, "Localized states in a film-dragging experiment," *Phys. Rev. E* **48**, 2704 (1993).

²⁴M. J. Karweit and S. Corrsin, "Observations of cellular patterns in a partly filled, horizontal cylinder," *Phys. Fluids* **18**, 111 (1975).

²⁵O. A. M. Boote and P. J. Thomas, "Effects of granular additives on transition boundaries between flow states of rimming flows," *Phys. Fluids* **11**, 2020 (1999).

²⁶M. Tirumkudulu, A. Mileo, and A. Acrivos, "Particle segregation in monodisperse sheared suspensions in a partially filled rotating horizontal cylinder," *Phys. Fluids* **12**, 1615 (2000).

²⁷E. Fried, A. Q. Shen, and S. T. Thoroddsen, "Wave patterns in a thin layer of sand within a rotating horizontal cylinder," *Phys. Fluids* **10**, 10 (1998).

²⁸J. A. Moriarty, L. W. Schwartz, and E. O. Tuck, "Unsteady spreading of thin liquid films with small surface tension," *Phys. Fluids A* **3**, 733 (1991).

²⁹H. Lamb, *Hydrodynamics* (Dover, New York, 1932).

³⁰S. G. Yiantsios and B. G. Higgins, "Rayleigh-Taylor instability in thin viscous films," *Phys. Fluids A* **1**, 1484 (1989).

³¹J. R. de Bruyn, "Crossover between surface tension and gravity-driven instabilities of a thin fluid layer on a horizontal cylinder," *Phys. Fluids* **9**, 1599 (1997).

³²F. Bashforth and J. C. Adams, *An Attempt to Test the Theories of Capillary Action* (Cambridge University Press, New York, 1883).

³³C. D. Hodgman, *CRC Handbook of Chemistry and Physics*, 36th ed. (CRC, Cleveland, 1954).

³⁴M. A. Spaid and G. M. Homsy, "Stability of Newtonian and viscoelastic dynamic contact lines," *Phys. Fluids* **8**, 460 (1996).

³⁵M. H. Eres, L. W. Schwartz, and R. V. Roy, "Fingering phenomena for driven coating films," *Phys. Fluids* **12**, 1278 (2000).

³⁶L. W. Schwartz, "Viscous flows down an inclined plane: Instability and finger formation," *Phys. Fluids A* **1**, 443 (1989).

³⁷A. Q. Shen, "Granular fingering patterns in horizontal rotating cylinders," *Phys. Fluids* **14**, 462 (2002).

³⁸N. N. Yanenko, *Metod Drobnykh Shagov Resheniya Mnogomernykh Zadach Matematicheskoi Fiziki*, The Method of Fractional Steps, edited by M. Holt (Springer, New York, 1971).

³⁹P. L. Evans, "Mathematical and numerical investigations of coating flows," Ph.D. thesis, University of Delaware, 2000.